

A 2DH hybrid Boussinesq-NSWE solver for near-shore hydrodynamics

F.M. Judge^{a,*}, J. Orszaghova^b, P.H. Taylor^{b,c}, A.G.L. Borthwick^a

^a Institute for Energy Systems, School of Engineering, The University of Edinburgh, UK

^b Faculty of Engineering and Mathematical Sciences, University of Western Australia, Australia

^c Keble College, University of Oxford, UK

ARTICLE INFO

Keywords:

Boussinesq
Shallow water
Finite differences
Finite volume
Nearshore circulation
Focused wave group

ABSTRACT

This paper presents a numerical model that simulates the nearshore circulation and the propagation of waves in two horizontal dimensions (2DH) across the coastal zone, from intermediate depth to zero depth. Pre-breaking, wave propagation is calculated using a Boussinesq equation set with enhanced dispersion characteristics, discretised using second-order central differences and solved using the conjugate gradient method with fourth order Runge-Kutta time integration. In the breaker zone, the Boussinesq dispersive terms are gradually switched off, and the resulting non-linear shallow water equations solved using a finite volume MUSCL-Hancock scheme with an HLLC approximate Riemann solver. Broken waves are treated as hydraulic bores. A wetting and drying algorithm models the moving wet/dry front at the shore. Waves are generated by a line of independently moving piston paddles which are represented through a linear mapping, stretching and compressing the grid in the region of the paddles. Model verification tests include wave sloshing in a frictionless basin, seiching in a parabolic basin with bed friction, solitary wave propagation over a horizontal bed, and the interaction of a solitary wave with a conical island. After calibration, the model simulates the generation of wave-induced currents by regular waves as they interact with sinusoidal and tricuspid beaches, and the propagation of a unidirectional focused wave group over a plane beach. Results are compared against previously published laboratory data. The validation tests confirm that the 2DH model reproduces several important coastal hydrodynamic phenomena including wave-induced currents and multi-component wave packets. The model can thus be used to replicate wave basin experiments, and could be extended to multi-directional waves, leading to a better understanding of hydrodynamic processes in shallow coastal waters.

1. Introduction

The Boussinesq equations (originally formulated by [Boussinesq \(1872\)](#)) represent an inviscid depth-averaged approximation of the Navier-Stokes equations. Over the past 50 years, Boussinesq-type models have become increasingly popular, due to their ability to represent adequately the main physical processes at the shore, while remaining relatively computationally efficient, compared to Navier-Stokes CFD solvers.

Early Boussinesq models based on the classical equations derived by [Peregrine \(1967\)](#) were limited to modelling very long waves, because of the weakly nonlinear, weakly dispersive nature of the governing equations, i.e. $O(\mu^2) = O(\varepsilon) < < 1$, where the dispersion parameter μ is the ratio of mean water depth to wavelength and the nonlinearity parameter ε is the ratio of the wave amplitude to mean water depth. [Madsen and Sørensen \(1992\)](#) improved the dispersive properties of the classical equations by applying a linear operator to the momentum

equation that resulted in higher-order dispersive contributions, while retaining only third-order derivatives. This led to an equation set valid for relative water depth up to $\mu = 0.5$. [Nwogu \(1993\)](#) also achieved improved dispersion characteristics without increasing the order of the governing equations, by formulating the equations in terms of a chosen reference velocity (evaluated at a specific depth) rather than a depth-averaged velocity. [Wei et al. \(1995\)](#), [Madsen and Schäffer \(1998\)](#), and [Gobbi et al. \(2000\)](#) among others, further extended the validity of Boussinesq-type equations by developing fully nonlinear models where $O(\varepsilon) = 1$. [Agnon et al. \(1999\)](#) were the first to achieve the same accuracy in nonlinear properties as in dispersion properties. The model was further enhanced by [Madsen et al. \(2003\)](#) who achieved a more accurate vertical velocity profile for a mildly sloping bed. The later model of [Madsen et al. \(2006\)](#) is valid for both fully nonlinear and highly dispersive waves propagating over rapidly changing bathymetry.

As most Boussinesq-type models are based on the assumption of irrotational flow, they cannot model wave breaking, and must be

* Corresponding author.

E-mail address: frances.judge@ucc.ie (F.M. Judge).

modified to account for the associated energy dissipation. The main approaches to this are the surface roller model and the eddy-viscosity model. The surface roller concept, stemming from the work of Svendsen (1984), forms the basis of models proposed by Schäffer et al. (1993) and Madsen et al. (1997). The eddy-viscosity approach to wave breaking introduces a diffusive-type term in the momentum equation and has been implemented in one-dimension by Karambas and Koutitas (1992) and in two-dimensions by Chen et al. (2000). Brigandt et al. (2004) apply a rotational flow approach to a fully nonlinear Boussinesq-type model, in which the eddy viscosity varies over the water column. This requires the numerical solution of the vorticity transport equation. The semi-integrated model of Antuono and Brocchini (2013) and Antuono et al. (2017) follows a similar approach. An alternative approach to wave breaking is to use a hybrid model based on Boussinesq-type equations pre-breaking and the shallow water equations post-breaking. This approach is adopted in the present research study, and builds on previous research by Borthwick et al. (2006), Orszaghova (2011), and Orszaghova et al. (2012). Hybrid Boussinesq-NSWE numerical models have also been proposed by Tonelli and Petti (2009), Tonelli and Petti (2012), Shi et al. (2012), and McCabe et al. (2013).

Before computer technology advanced to the stage where Boussinesq modelling of the surf-zone became possible, most models of wave-induced circulation in the nearshore zone were based on period-averaged, depth-integrated conservation laws of mass and momentum. Early work on modelling wave-current interaction using Boussinesq-type equations was carried out by Yoon and Liu (1989). Chen et al. (2000) developed a two-dimensional model of wave-induced nearshore circulation based on the fully nonlinear Boussinesq equations and achieved satisfactory results for waves breaking over rapidly changing bathymetry. Chen et al. (1999) applied the model to a rip current system.

Focused wave groups represent an efficient means for coastal engineers to model realistic large wave events at the coast, either numerically or in the laboratory, and estimate run-up and overtopping. Other alternatives are regular waves, which being regular sinusoids do not properly model a realistic sea state, or irregular (random) wave simulations. The major drawback of the latter is the length of simulation required to produce an extreme event, which leads to problems of repeated wave reflections in laboratory experiments and a heavy computational load for numerical models. NewWave is a methodology that ensures the focused wave group corresponds to the average shape of the largest wave event in a Gaussian sea state, which is imperative for accurate calculations of run-up and overtopping. The theory behind NewWave was first developed by Lindgren (1970) and independently by Boccotti (1983). Tromans et al. (1991) applied the concept to deep water applications. Jonathan and Taylor (1997) verified NewWave against large waves in deep water whereas Taylor and Williams (2004) undertook a similar exercise for waves in intermediate depth. Whittaker et al. (2016) confirm the validity of NewWave in relatively shallow coastal waters.

The one-dimensional hybrid numerical solver developed by Orszaghova (2011) has proved to be a computationally efficient and accurate tool for modelling nearshore wave propagation, run-up and overtopping (Orszaghova et al., 2012) (Fitzgerald et al., 2016). This paper extends Orszaghova's solver to two horizontal dimensions (2DH) which facilitates the investigation of more complicated wave-wave and wave-shoreline interactions, in particular those interactions that lead to wave-induced nearshore currents. Thus, a 2DH model is presented which solves the enhanced Boussinesq equation set of Madsen and Sørensen (1992) pre-breaking and the nonlinear shallow water equations post-breaking. Although the Madsen and Sørensen equations are relatively simple in comparison with the more sophisticated, higher-order Boussinesq equation sets, simplicity is a key consideration for the development of a numerical model that does not necessarily require high-performance computing resources to be a useful tool to the coastal engineer. Waves in the model are generated by a system of

independently moving piston-type paddles. A linear mapping is applied in the region of the paddles, and the governing equations are solved on the transformed, fixed domain, to overcome the problem of a time-varying domain when the paddles are in motion. The wave generation mechanism enables full replication of laboratory experiments, including the generation of multi-directional seas and their interaction with shorelines of different configurations.

2. Governing equations

2.1. Nonlinear shallow water equations

The nonlinear shallow water equations implemented in the numerical model include the effects of bed friction and deviatoric stresses, and are given by

$$\frac{\partial \zeta}{\partial t} + \frac{\partial q_x}{\partial x} + \frac{\partial q_y}{\partial y} = 0, \quad (1a)$$

$$\frac{\partial q_x}{\partial t} + gd\frac{\partial \zeta}{\partial x} + \frac{\partial}{\partial x}\left(\frac{q_x^2}{d}\right) + \frac{\partial}{\partial y}\left(\frac{q_x q_y}{d}\right) = -\tau_{bx} + \left(\frac{\partial}{\partial x}(dT_{xx}) + \frac{\partial}{\partial y}(dT_{xy})\right) \quad (1b)$$

and

$$\frac{\partial q_y}{\partial t} + gd\frac{\partial \zeta}{\partial y} + \frac{\partial}{\partial y}\left(\frac{q_y^2}{d}\right) + \frac{\partial}{\partial x}\left(\frac{q_x q_y}{d}\right) = -\tau_{by} + \left(\frac{\partial}{\partial x}(dT_{xy}) + \frac{\partial}{\partial y}(dT_{yy})\right) \quad (1c)$$

where ζ is the free surface elevation above the still water level, d is the total water depth, h is the still water depth, and g is the acceleration due to gravity. $q_x = \int_{-h}^{\zeta} u \, dz$ and $q_y = \int_{-h}^{\zeta} v \, dz$ are the fluxes in the x - and y -directions respectively, in which u and v are the depth-integrated velocities. τ_{bx} and τ_{by} are bed friction stresses per unit water density, estimated empirically from

$$\tau_{bx} = C_f u \sqrt{u^2 + v^2} \quad \text{and} \quad \tau_{by} = C_f v \sqrt{u^2 + v^2}, \quad (2)$$

in which C_f is the bed roughness coefficient and T_{xx} , T_{xy} and T_{yy} are effective stress terms. The effective stresses are the deviatoric stresses, grouped together with the stresses that arise from the non-uniformity of the vertical velocity profile as a result of the depth-integration process. They consist of three components: a molecular viscous stress, a Reynolds stress due to turbulent fluctuating velocity components, and a stress related to the non-uniformity of the vertical velocity profile. For most flow situations, the first and third components are significantly smaller than the Reynolds stresses, and can be neglected. The method of evaluating the Reynolds stresses is referred to as the turbulence model. The Boussinesq eddy viscosity concept forms the basis of many turbulence models, and expresses the Reynolds stresses in terms of the gradients of the time-averaged velocity components, giving

$$T_{xx} = 2\varepsilon \frac{\partial \bar{u}}{\partial x}, \quad T_{xy} = \varepsilon \left(\frac{\partial \bar{v}}{\partial x} + \frac{\partial \bar{u}}{\partial y} \right), \quad \text{and} \quad T_{yy} = 2\varepsilon \frac{\partial \bar{v}}{\partial y}, \quad (3)$$

in which ε is the eddy viscosity. This is the simplest possible turbulence model, dating back to Reynolds and Prandtl, and is implemented in the present model, following Borthwick and Barber (1992). The value of ε can be calculated from constant or depth-averaged eddy viscosity models.

2.1.1. Stage-discharge formulation

Formulation in terms of the free surface elevation ζ and the still water depth h presents difficulties when applying the shallow water equations to problems that involve a wet-dry interface, because both h and ζ are difficult to define at the interface and in dry areas. Problems also arise when there are discontinuous bodies of water, such as ponds at different elevations. This problem manifests itself during coastal overtopping, when the mean water levels either side of a wall or bank

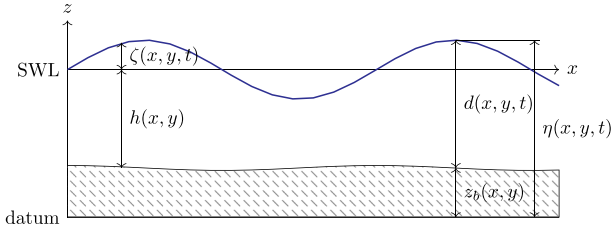


Fig. 1. Definition sketch.

may be quite different after an inundation event. Following earlier work by Rogers et al. (2003), Liang and Borthwick (2009) split the free surface gradient terms as follows in the x -direction:

$$gh \frac{\partial \zeta}{\partial x} = \frac{g}{2} \frac{\partial(\eta^2 - 2z_b \eta)}{\partial x} + g\eta \frac{\partial z_b}{\partial x}, \quad (4)$$

and similarly in the y -direction, where z_b is the bed elevation above a horizontal datum, and $\eta = z_b + h + \zeta$. The splitting can be derived by examining the momentum balance across a vertical element of liquid extending from the bed to the free surface in the x -direction (and of unit width in the y -direction). For details of the full derivation, see Liang and Borthwick (2009).

From Fig. 1 it can be seen that because η is measured relative to the datum, it is always consistently defined. Formulation in terms of η and z_b means that the model can then deal with discontinuous bodies of water, such as may occur when a seawall is overtopped. Flows due to inundation beyond a sea defence can then be handled by the numerical model. The system of shallow water equations implemented in the numerical model thus becomes

$$\frac{\partial \mathbf{u}}{\partial t} + \frac{\partial \mathbf{f}}{\partial x} + \frac{\partial \mathbf{g}}{\partial y} = \mathbf{s}, \quad (5)$$

where

$$\begin{aligned} \mathbf{u} &= \begin{bmatrix} \eta \\ q_x \\ q_y \end{bmatrix}, \quad \mathbf{f} = \begin{bmatrix} q_x \\ \frac{q_x^2}{d} + \frac{1}{2}g(\eta^2 - 2\eta z_b) \\ \frac{q_x q_y}{d} \end{bmatrix}, \quad \mathbf{g} = \begin{bmatrix} q_y \\ \frac{q_x q_y}{d} \\ \frac{q_y^2}{d} + \frac{1}{2}g(\eta^2 - 2\eta z_b) \end{bmatrix} \text{ and} \\ \mathbf{s} &= \begin{bmatrix} 0 \\ -\tau_{bx} - g\eta \frac{\partial z_b}{\partial x} + (\frac{\partial}{\partial x}(dT_{xx}) + \frac{\partial}{\partial y}(dT_{xy})) \\ -\tau_{by} - g\eta \frac{\partial z_b}{\partial y} + (\frac{\partial}{\partial x}(dT_{xy}) + \frac{\partial}{\partial y}(dT_{yy})) \end{bmatrix}. \end{aligned} \quad (6)$$

2.2. Boussinesq equations

Including the effects of bed friction and eddy viscosity, and formulated in terms of (η, q_x, q_y) , the enhanced Boussinesq equation set of Madsen and Sørensen (1992) implemented in the numerical model is as follows:

$$\frac{\partial \eta}{\partial t} + \frac{\partial q_x}{\partial x} + \frac{\partial q_y}{\partial y} = 0, \quad (7a)$$

$$\begin{aligned} \frac{\partial q_x}{\partial t} + \frac{\partial(\frac{q_x^2}{d})}{\partial x} + \frac{g}{2} \frac{\partial \eta^2}{\partial x} - g \frac{\partial(\eta z_b)}{\partial x} + \frac{\partial(\frac{q_x q_y}{d})}{\partial y} &= -\tau_{bx} - g\eta \frac{\partial z_b}{\partial x} \\ + (\frac{\partial}{\partial x}(dT_{xx}) + \frac{\partial}{\partial y}(dT_{xy})) + \Psi_1, \end{aligned} \quad (7b)$$

and

$$\begin{aligned} \frac{\partial q_y}{\partial t} + \frac{\partial(\frac{q_y^2}{d})}{\partial y} + \frac{g}{2} \frac{\partial \eta^2}{\partial y} - g \frac{\partial(\eta z_b)}{\partial y} + \frac{\partial(\frac{q_x q_y}{d})}{\partial x} &= -\tau_{by} - g\eta \frac{\partial z_b}{\partial y} \\ + (\frac{\partial}{\partial x}(dT_{xy}) + \frac{\partial}{\partial y}(dT_{yy})) + \Psi_2, \end{aligned} \quad (7c)$$

where (Ψ_1, Ψ_2) are dispersive terms, given by

$$\begin{aligned} \Psi_1 &= (B + \frac{1}{3})h^2(\frac{\partial^3 q_x}{\partial x^2 \partial t} + \frac{\partial^3 q_y}{\partial x \partial y \partial t}) + Bgh^3(\frac{\partial^3 \eta}{\partial x^3} + \frac{\partial^3 \eta}{\partial x \partial y^2}) \\ &+ h \frac{\partial h}{\partial x}(\frac{1}{3} \frac{\partial^2 q_x}{\partial x \partial t} + \frac{1}{6} \frac{\partial^2 q_y}{\partial y \partial t} + 2Bgh \frac{\partial^2 \eta}{\partial x^2} + Bgh \frac{\partial^2 \eta}{\partial y^2}) + h \frac{\partial h}{\partial y}(\frac{1}{6} \frac{\partial^2 q_y}{\partial y \partial t} + Bgh \frac{\partial^2 \eta}{\partial x \partial y}), \end{aligned} \quad (8a)$$

and

$$\begin{aligned} \Psi_2 &= (B + \frac{1}{3})h^2(\frac{\partial^3 q_y}{\partial y^2 \partial t} + \frac{\partial^3 q_x}{\partial x \partial y \partial t}) + Bgh^3(\frac{\partial^3 \eta}{\partial y^3} + \frac{\partial^3 \eta}{\partial x^2 \partial y}) \\ &+ h \frac{\partial h}{\partial y}(\frac{1}{3} \frac{\partial^2 q_y}{\partial y \partial t} + \frac{1}{6} \frac{\partial^2 q_x}{\partial x \partial t} + 2Bgh \frac{\partial^2 \eta}{\partial y^2} + Bgh \frac{\partial^2 \eta}{\partial x^2}) + h \frac{\partial h}{\partial x}(\frac{1}{6} \frac{\partial^2 q_x}{\partial y \partial t} + Bgh \frac{\partial^2 \eta}{\partial x \partial y}), \end{aligned} \quad (8b)$$

in which B is the Boussinesq linear dispersion coefficient. By setting $B = \frac{1}{15}$, the embedded linear dispersion relation of (7) is equivalent to a [2][2] Padé expansion of the exact linear dispersion relation, $\omega^2 = gk \tanh(kh)$. Setting $B = 0$ reverts back to Peregrine's classical Boussinesq equation set.

3. Numerical implementation

3.1. Computational grid and domain mapping

In the numerical model, the physical domain is represented by a two-dimensional, rectangular grid of length L_x and width L_y . Waves are generated by a line of i_{max} independently moving piston paddles along the western boundary of the basin (see Fig. 2). Note that a row-column indexing notation is used, whereby the i, j subscripts of a point p_{ij} on the grid represent the indices of points in the y - and x -directions respectively. Initially, when the paddles are at rest in the zero position, the Cartesian coordinates of the underlying uniform grid are given by

$$(x_j, y_i) = ((j - 1)\Delta x, (i - 1)\Delta y), \quad (9)$$

where $\Delta x = L_x/(i_{max} - 1)$ and $\Delta y = L_y/(i_{max} - 1)$, for $j = 1..i_{max}$ and $i = 1..i_{max}$. Δx and Δy are the spacings between grid points in the x - and y -directions respectively.

The length of the basin varies with time when the paddles are moving. To deal with this, the region governed by the Boussinesq equations is divided into two zones: the moving domain and the fixed domain. The moving domain is of variable length $b_i(t)$ in the x -direction and fixed width, L_y . At $t = 0$, all of the paddles are in the zero position, and the initial x -dimension of the moving domain is given by a fixed length, $b_i(t = 0)$, herein referred to as b_0 , which contains a fixed number of grid points, \tilde{B} , in the x -direction. The length of b_0 , and consequently the value of \tilde{B} is chosen depending on the problem under consideration. A similar approach is adopted to that of (Orszag (2011)), whereby b_0 is set to be approximately 10 times the maximum paddle sweep.

When the paddles at the western boundary are in motion, the lattice of grid points that define the paddle domain stretches and compresses as the paddles move. In order to avoid re-meshing in this region at every time step, a transformation is used to map the moving grid onto a fixed computational grid to facilitate the solution of the governing equations. As the paddles are confined to the western edge of the tank and can only move in the x -direction, the mapping employed is a function of x only. Each moving row of grid points in the paddle domain is mapped onto a fixed row with points distributed evenly on the interval $(-1, 1)$, with spacing, (see Fig. 3) $\Delta \tilde{x} = 2/(\tilde{B} - 1)$.

The initial length of the paddle domain is given by a fixed length, b_0 . As the paddles move, each row, i , of the grid has a variable length $b_i(t) = b_0 - x_{p_i}(t)$, where $x_{p_i}(t)$ is the paddle displacement time series for the i -th paddle. The transformation from the moving (x, y, t) domain to the fixed $(\tilde{x}, \tilde{y}, \tilde{t})$ domain, is based on the following linear stretching mapping:

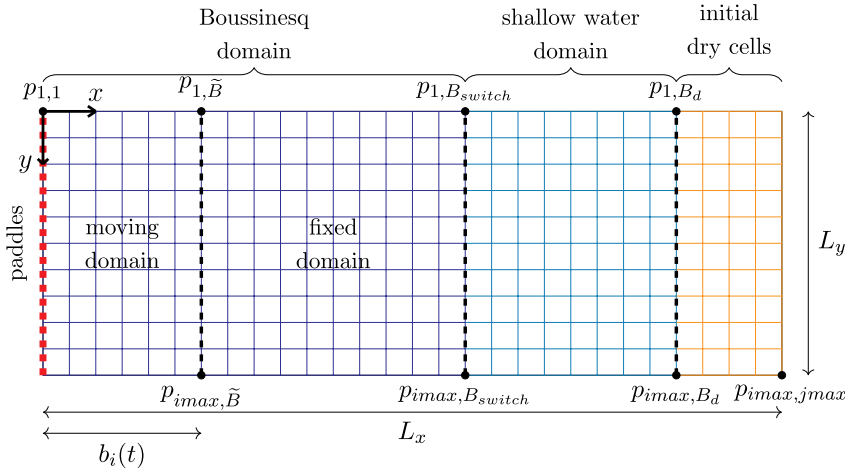


Fig. 2. Sample basin layout.

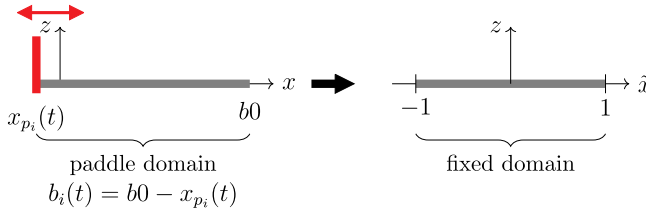


Fig. 3. Paddle domain transformation applied to the moving domain.

$$\tilde{x} = -1 + 2\left(\frac{x - x_{p_i}(t)}{b_i(t)}\right). \quad (10)$$

Note that $\tilde{y} = y$ and $\tilde{t} = t$. Thus, $f(x, y, t) \rightarrow \tilde{f}(\tilde{x}, \tilde{y}, \tilde{t})$. The transformed basic derivative operators are derived by applying the chain rule, yielding

$$\frac{\partial}{\partial x} = \frac{2}{b_i(t)} \frac{\partial}{\partial \tilde{x}}, \quad \frac{\partial}{\partial y} = \frac{\partial}{\partial \tilde{y}}, \quad \text{and} \quad \frac{\partial}{\partial t} = \frac{\partial}{\partial \tilde{t}} + \frac{1}{b_i(t)} \frac{\partial b_i(t)}{\partial \tilde{t}} (1 - \tilde{x}) \frac{\partial}{\partial \tilde{x}}. \quad (11)$$

Higher order and mixed derivatives are obtained through careful combination of the above operators. Application of the transformation in (10) to (7), via the transformed derivative operators, results in the mapped Boussinesq equation set. Both sets of equations (the transformed set in the vicinity of the paddles, and the untransformed equations given by (7) in the rest of the Boussinesq domain), are solved numerically in the same way, as described in Section 3.2.

3.2. Numerical solution of the Boussinesq equations

3.2.1. Finite difference discretisation

The Boussinesq equations are discretised using a second-order centred finite difference scheme. This involves a three point stencil for first and second derivatives and a five point stencil for higher order derivatives. The stencils for the spatial cross-derivative terms, $\partial^2/\partial x \partial y$, $\partial^3/\partial x^2 \partial y$ and $\partial^3/\partial x \partial y^2$, span three points in the x and y directions.

The finite difference expressions at the interface between the moving and fixed domains must be treated carefully, because different governing equation sets and grid spacing exist either side of $j = \tilde{B}$. At a point $p_{i,j}$, where $j = \tilde{B}$, the three-point stencil defining first and second derivatives and the five-point higher order stencils will span both regions. Where third-order derivatives are calculated at $j = \tilde{B} - 1$, or $j = \tilde{B} + 1$, the five-point stencil employed will again span both regions. Mixed derivative non-uniform stencils are obtained through careful combination of the non-uniform and uniform stencils. Expressions for the first and second-order stencils at $j = \tilde{B}$ are given in (12). Higher

order and mixed derivative stencils as well as the equivalent expressions at $j = \tilde{B} - 1$ and $j = \tilde{B} + 1$ have been omitted for brevity. Note that $b_i(t)$ is abbreviated to b_i .

$$f_{\tilde{x}}(p_{i,j=\tilde{B}}) = -\frac{1}{\Delta \tilde{x}} \left(\frac{b_0}{b_i + b_0} \right) f_{i,\tilde{B}-1} - \frac{1}{\Delta \tilde{x}} \left(\frac{b_i - b_0}{b_0} \right) f_{i,\tilde{B}} + \frac{1}{\Delta \tilde{x}} \left(\frac{b_i^2}{b_0(b_i + b_0)} \right) f_{i,\tilde{B}+1}, \quad (12a)$$

$$f_{\tilde{x}\tilde{x}}(p_{i,j=\tilde{B}}) = \frac{1}{\Delta \tilde{x}^2} \left(\frac{2b_i}{b_i + b_0} \right) f_{i,\tilde{B}-1} - \frac{1}{\Delta \tilde{x}^2} \left(\frac{2b_i}{b_0} \right) f_{i,\tilde{B}} + \frac{1}{\Delta \tilde{x}^2} \left(\frac{2b_i^2}{b_0(b_i + b_0)} \right) f_{i,\tilde{B}+1}. \quad (12b)$$

3.2.2. Time integration and conjugate gradient solver

The discretised systems to be solved can be written as

$$\eta_t = \mathbf{a}(\eta, q_x, q_y) \quad (13a)$$

and

$$\mathbf{AQ}_t = \mathbf{b}(\eta, q_x, q_y) \quad (13b)$$

where η represents the vector of values of η , and \mathbf{Q} represents a vector containing values of q_x and q_y at each grid point within the Boussinesq domain. \mathbf{a} is the vector of non-time-dependent terms of (7a), and \mathbf{b} is a similar vector representing the non-time-dependent terms of equations (7b) and (7c). Non-time-dependent terms refer to all terms that do not contain a time derivative of the conserved variables, i.e. $\partial \eta / \partial t$, $\partial q_x / \partial t$, and $\partial q_y / \partial t$. Thus \mathbf{Q} and \mathbf{b} have double the number of values of η and \mathbf{a} . \mathbf{A} is a matrix of coefficients resulting from the discretisation of the time-dependent terms of equations (7b) and (7c), and is of size $(m \times m)$, where $m = imax \times (\tilde{B}_{switch} - 2) \times 2$. System (13) is integrated forward in time using a fourth-order Runge-Kutta algorithm (RK4). At each stage of the RK4 algorithm, a linear system of the form $\mathbf{Ax} = \mathbf{b}$ must be solved, where \mathbf{x} is the vector of $\frac{\partial q_x}{\partial t}$ and $\frac{\partial q_y}{\partial t}$ at each grid point. \mathbf{A} and \mathbf{b} are as described in the previous section. The matrix \mathbf{A} is a real, symmetric, positive definite, sparse banded matrix. The conjugate gradient method, originally proposed by Hestenes and Stiefel (1952), is suited to the numerical solution of such a system. It stems from the method of steepest descent, but instead of searching in the direction in which the function to be minimised, f , decreases most quickly, the search directions used are \mathbf{A} -orthogonal to each other. Two vectors, \mathbf{d}_i and \mathbf{d}_j are said to be \mathbf{A} -orthogonal, or conjugate, if $\mathbf{d}_i^T \mathbf{Ad}_j = 0$. Given the inputs \mathbf{A} , \mathbf{b} and a starting estimate of the solution, \mathbf{x} (typically zero), the method of conjugate gradients as summarised in Shewchuk (1994) is as follows:

$$\begin{aligned}
n &= 0 \\
\mathbf{d}_n &= \mathbf{r}_n = \mathbf{b} - \mathbf{Ax}_n \\
\delta_0 &= \delta_{new} = \mathbf{r}_n^T \mathbf{r}_n \\
\text{While } n < n_{max} \text{ and } \delta_{new} > \epsilon^2 \delta_0 \\
\alpha_n &= \frac{\mathbf{r}_n^T \mathbf{r}_n}{\mathbf{d}_n^T \mathbf{A} \mathbf{d}_n} \\
\mathbf{x}_{n+1} &= \mathbf{x}_n + \alpha_n \mathbf{d}_n \\
\mathbf{r}_{n+1} &= \mathbf{r}_n - \alpha_n \mathbf{A} \mathbf{d}_n \\
\delta_{old} &= \delta_{new} \\
\delta_{new} &= \mathbf{r}_{n+1}^T \mathbf{r}_{n+1} \\
\beta &= \frac{\mathbf{r}_{n+1}^T \mathbf{r}_{n+1}}{\mathbf{r}_n^T \mathbf{r}_n} \\
\mathbf{d}_{n+1} &= \mathbf{r}_{n+1} + \beta \mathbf{d}_n \\
n &= n + 1
\end{aligned} \tag{14}$$

where \mathbf{d} is the vector of search directions, \mathbf{r} is the residual, n is the iteration, and ϵ is the error tolerance. When the algorithm is fully converged, i.e. the minimum has been reached, the residual is equal to zero. In practice however, the algorithm stops when the norm of the residual falls below the specified tolerance, or the maximum number of iterations, n_{max} , is reached.

For ease of numerical implementation, the dispersive terms in the Boussinesq momentum equations are neglected at the points closest to the paddles ($j = 1, 2$). It is assumed that over this short distance, the lack of dispersion is not significant. A first-order forward difference discretisation of the resulting shallow water equations is used at the paddle faces ($j = 1$), with a second-order centred difference scheme implemented one column of grid points away from the paddles in the x -direction ($j = 2$). Second-order discretisation of the full Boussinesq equation set begins at $j = 3$.

3.2.3. Boundary conditions for the Boussinesq region

At the start of each time step, the flux in the x -direction, q_x , at the paddle faces ($j = 1$) is updated to match the paddle motion,

$$q_{x_{i,1}} = d_{i,1} (x_{p_i}(t))_t, \tag{15}$$

where d is the local water depth at the paddle, and $(x_{p_i}(t))_t$ is the velocity of the i^{th} paddle at the current time step. Slip conditions are assumed along the paddle faces. Therefore the steps that result along the $j = 1$ boundary due to the motion of the paddles in the x -direction are not considered. It is assumed that the relative motion of adjacent paddles is sufficiently small not to impact on the results in a significant way.

The northern and southern boundaries of the domain ($i = 1$ and $i = imax$; $j = 1, \dots, B_{switch}$), are vertical solid walls. Since there can be no flux through the boundaries, $q_{y_{1,j}} = q_{y_{imax,j}} = 0$. Slip boundary conditions are implemented in the numerical model using ‘ghost’ grid points beyond the boundary, whereby

$$\begin{aligned}
\eta_{0,j} &= \eta_{2,j}, & q_{x0,j} &= q_{x2,j}, & q_{y0,j} &= -q_{y2,j} \\
\eta_{-1,j} &= \eta_{3,j}, & q_{x-1,j} &= q_{x3,j}, & q_{y-1,j} &= -q_{y3,j} \\
\eta_{imax+1,j} &= \eta_{imax-1,j}, & q_{ximax+1,j} &= q_{ximax-1,j}, & q_{yimax+1,j} &= -q_{yimax-1,j} \\
\eta_{imax+2,j} &= \eta_{imax-2,j}, & q_{ximax+2,j} &= q_{ximax-2,j}, & q_{yimax+2,j} &= -q_{yimax-2,j}
\end{aligned} \tag{16}$$

In cases where the whole domain is solved by the Boussinesq equations, i.e. $B_{switch} = jmax$, no flow through the eastern boundary means that $q_{xi,jmax} = 0$ for $i = 1, \dots, imax$. Here, slip boundary conditions corresponding to vertical, solid walls must also be applied where, again, ghost cells are used.

$$\begin{aligned}
\eta_{i,jmax+1} &= \eta_{i,jmax-1}, & q_{xi,jmax+1} &= -q_{xi,jmax-1}, & q_{yi,jmax+1} &= q_{yi,jmax-1} \\
\eta_{i,jmax+2} &= \eta_{i,jmax-2}, & q_{xi,jmax+2} &= -q_{xi,jmax-2}, & q_{yi,jmax+2} &= q_{yi,jmax-2}
\end{aligned} \tag{17}$$

3.2.4. Smoothing of the updated solution

A feature of iterative solvers such as the conjugate gradient method, is the accumulation of floating point error in the solution. These errors can grow rapidly and lead to saw-tooth instabilities that result in the model crashing. To mitigate against these instabilities, as well as the accumulation of error due to the first-order discretisation used at the paddle face, numerical smoothing is applied in the moving paddle domain. This takes the form of a 5-point filter applied in the y -direction parallel to the paddle faces. It is given by

$$\eta_{i,j}^{smooth} = \frac{1}{20} (\eta_{i-2,j} + 4\eta_{i-1,j} + 10\eta_{i,j} + 4\eta_{i+1,j} + \eta_{i+2,j}), \tag{18}$$

where $\eta_{i,j}^{smooth}$ represents the smoothed value of η at each grid point in the paddle domain, calculated using the updated values of η at the end of every time step. The same filter is applied to the fluxes q_x and q_y . Applying a filter in this way also minimises the potential for instability due to the assumption of slip conditions along the paddle faces, as described in the previous section.

3.3. Numerical solution of the nonlinear shallow water equations

3.3.1. Finite volume solver

The nonlinear shallow water equations are used to model broken waves propagating as bores as well as being implemented in areas of shallow water ($d/\lambda < 0.05$, where d is the local water depth and λ is the wavelength). Thus a numerical scheme with shock-capturing capabilities is necessary to evolve discontinuous, steep-fronted flows. When discontinuities are present, the derivatives approximated by finite difference methods cannot be calculated. Hence, a finite volume method is used, which is based on the integral form of (5), given by

$$\frac{\partial}{\partial t} \int_{\Omega} \mathbf{u} \, d\Omega + \int_{\Omega} \left(\frac{\partial \mathbf{f}}{\partial x} + \frac{\partial \mathbf{g}}{\partial y} \right) d\Omega = \int_{\Omega} \mathbf{s} \, d\Omega \tag{19}$$

where \mathbf{u} , \mathbf{f} , \mathbf{g} and \mathbf{s} are given by (6) and Ω represents the volume element. In this research, the Godunov-type finite volume solver outlined by Liang and Borthwick (2009) is implemented, with an HLLC approximate Riemann solver used to evaluate the fluxes across the interfaces between volumes where discontinuities might be present. Godunov, or upwind methods, use wave propagation information to construct the numerical scheme. The solver operates on a regular grid, with the coordinates of the centres of the grid cells or volumes given by (x_j, y_i) for $j = B_{switch} + 1, \dots, B_d$ and $i = 1, \dots, imax$. In this scheme, the time-marching formula is given by

$$\mathbf{u}_{i,j}^{n+1} = \mathbf{u}_{i,j}^n - \frac{\Delta t}{\Delta x} (\mathbf{f}_E - \mathbf{f}_W) - \frac{\Delta t}{\Delta y} (\mathbf{g}_N - \mathbf{g}_S) + \Delta t s_{i,j} \tag{20}$$

where the subscript i, j refers to the cell index, the superscript n represents the time level, Δt is the time step, Δx and Δy are the grid spacings, and \mathbf{f}_E , \mathbf{f}_W , \mathbf{g}_N and \mathbf{g}_S are the fluxes through east, west, north and south faces respectively of each cell.

Following (Liang and Borthwick, 2009), the MUSCL-Hancock predictor-corrector method is adopted to integrate the equations forward in time. This method achieves second-order accuracy in time and space.

3.3.2. Boundary conditions for the shallow water equations

If the eastern end of the basin is inundated, and the nonlinear shallow water equations are applied in this region, ghost cells are utilised beyond the eastern wall of the tank in a similar way as in the Boussinesq region. Given that the conserved variables are calculated at cell centres in the finite volume solver, the eastern boundary of the basin exists at the interface between cells, giving rise to the boundary conditions

$$\eta_{i,jmax+1} = \eta_{i,jmax}, \quad q_{xi,jmax+1} = -q_{xi,jmax}, \quad q_{yi,jmax+1} = q_{yi,jmax}. \tag{21}$$

Similarly, the boundary conditions for the northern and southern boundaries of the shallow water domain are given by

$$\begin{aligned} \eta_{0,j} &= \eta_{1,j}, & q_{x0,j} &= q_{x1,j}, & q_{y0,j} &= -q_{y1,j} \\ \eta_{imax+1,j} &= \eta_{imax,j}, & q_{ximax+1,j} &= q_{ximax,j}, & q_{yimax+1,j} &= -q_{yimax,j} \end{aligned} \quad (22)$$

where $j = B_{switch+1}, \dots, B_d$.

3.3.3. Wetting and drying

The method described by Liang and Borthwick (2009) is invoked where a wet/dry front exists towards the eastern end of the basin. In this approach to wetting and drying, the local bed slope is modified to avoid spurious flow in dry cells. In general, dry cells are excluded from the computational domain unless they are about to be flooded, i.e., if a cell is dry but has a bed level below that of a wet neighbour. The moving shoreline is thus automatically tracked by the finite volume solver.

Following (Liang and Borthwick, 2009) and (Brufau et al., 2002) any cell with water depth less than the critical value (generally 1 mm for laboratory scale simulations) is automatically dried out and the fluxes set to zero. The small amount of water that was present is added to a wet adjacent cell to ensure mass conservation. In some cases, for example when the slope is steep, the model may predict that more water than is actually available will flow out of the cell of interest, causing a negative water depth. In this situation, the depth is set to zero and water is subtracted from the adjacent cell containing the most water, again ensuring mass is conserved. In both cases, the fluxes, q_x and q_y in the adjacent cell are adjusted to ensure the velocities remain the same as before.

It should be noted that automatically drying out cells with water depths below a critical value results in a shoreline position that differs from the theoretical shoreline. Antuono et al. (2012) show that in depth-averaged models that incorporate a Chézy-type frictional formulation, where $C_f \neq 0$ the difference between the theoretical and fictitious shorelines grows linearly with time. This is due to the generation of a thin layer of water on the beach face which has a weak influence on the water dynamics in this area.

3.4. Wave breaking and the interface between the Boussinesq and shallow water domains

The 2DH model implements the enhanced Boussinesq equations (7) pre-breaking where the modelled free surface is smooth. The nonlinear shallow water equations (5) are applied to shoaling waves, which allows them to shock up, break and propagate as bores. The energy dissipation that results from wave breaking is naturally handled by (5) due to the energy loss across the shock (see for example Section 2.7 of Johnson (1997)). In the numerical model, the switch from Boussinesq to shallow water equations to initiate wave breaking occurs when the slope of the free surface exceeds a critical threshold, given by

$$\Theta = \sqrt{\left(\frac{\partial \eta}{\partial x}\right)^2 + \left(\frac{\partial \eta}{\partial y}\right)^2}. \quad (23)$$

This calculation is performed at all points in the numerical domain at the beginning of each time step. The most offshore point where $\Theta > 0.4$, (approximately 22°) determines the breaking location. Orszaghova (2011) found that this value for the slope of the breaking wave worked well for the test cases considered in Orszaghova (2011), and as a result has also been implemented in the present research. Also following (Orszaghova, 2011), the switch point between equation sets, B_{switch} , is located a quarter wavelength offshore of this point. The wavelength of the shoaling wave that triggers the equation set switch is estimated by carrying out a down-crossing analysis in the x -direction, as waves are predominantly travelling in this direction. Therefore, the Boussinesq equations are applied offshore of the switch point, whereas the shallow water equations are applied at all points onshore of the switch. The switch is applied uniformly across the basin in the y -direction so that the interface between the Boussinesq and shallow water

domains is a straight line perpendicular to the side walls of the basin, as illustrated in Fig. 2. While this may appear to be an overly simplistic approach for a model that operates in two horizontal dimensions, it is sufficiently accurate for waves approaching the shore at a reasonably shallow angle ($\leq 30^\circ$ to the shore normal). A more sophisticated breaking criterion warrants further research.

The dispersion/shallowness parameter is also considered when determining the switch between the Boussinesq and shallow water equations. This parameter is defined as $\mu = \frac{d}{\lambda}$, where d is the local water depth and λ is the wavelength. Where λ cannot be easily determined, i.e. in an irregular wave field, it is represented by a typical horizontal length scale that is set by the user. This is set to 1.0 for the irregular waves presented in this research. Regardless of whether the switch between equation sets has been triggered by the free surface slope criterion, the shallow water equations are implemented in all areas where $\mu \leq \frac{1}{20}$, i.e. where dispersive effects are negligible. Bellotti and Brocchini (2002) show that dispersive contributions of $O(\mu^2)$ in Boussinesq-type equations disappear in the swash zone. Given that the shallow water equations are a subset of the Boussinesq equations, their use in this region is mathematically consistent.

To ensure a smooth transition between equation sets, the dispersive terms of the Boussinesq equations are gradually ramped down approaching B_{switch} . The ramping function is given by

$$f_{ramp} = \begin{cases} 1 & x < r_s, \\ \cos^2\left(\frac{\pi}{2} \frac{x - r_s}{x_{Bswitch} - r_s}\right) & r_s \leq x \leq x_{Bswitch}, \end{cases} \quad (24)$$

and is applied as a scaling function on the dispersive terms ((8a) and (8b)) in the ramping zone. r_s denotes the x -coordinate of the starting point of this zone, which is located half a wavelength offshore of $x_{Bswitch}$ in the x -direction. The ramping zone is applied uniformly across the basin in the y -direction. Thus, all dispersive terms have disappeared by $x_{Bswitch}$ and the shallow water equations are solved onshore of this point.

Where the switch between the Boussinesq and shallow water regions exists, an adjustment must be made to the Boussinesq solver at the interface. In the RK4 algorithm, the stage 4 calculation of the gradients of η , q_x and q_y at $x_{Bswitch}$ requires a five-point stencil of information in the x and y -directions. Therefore the stencil extends 2 points in the x -direction into the shallow water domain. Working the data requirements back to stage 1 of the RK4 algorithm, data extending to $x_{Bswitch+8}$ are required by the Boussinesq solver. These data are simply provided by solving the shallow water equations where $x_{Bswitch+1} \leq x \leq x_{Bswitch+8}$. In the coefficient matrix A , the main diagonal entries for these data from the shallow water region, $A_{i,j}$ where $i = j$, are set to unity, and all corresponding off-diagonal entries are set to zero.

4. Model verification tests

4.1. Evolution of sloshing waves in a closed basin

The evolution of symmetric sloshing waves in a closed square basin is considered to test the stability of the model and to verify the correct handling of the cross-derivative terms. The 2DH model results are compared to a linear analytical solution, calculated at points of interest in the basin. The test has also been considered by other researchers to verify numerical models (Wei and Kirby, 1995) (Jalali and Borthwick, 2017). The symmetric wave is of the form of an initial ‘hump’ of water shown in Fig. 4. It is defined as a two-dimensional Gaussian surface, described by the equation

$$\zeta_0(x, y) = H_0 \exp\left[-b\left(\left(x - \frac{L_x}{2}\right)^2 + \left(y - \frac{L_y}{2}\right)^2\right)\right] \quad (25)$$

where ζ_0 is the initial super-elevation of the water surface above an underlying still water depth h , L_x and L_y are the basin dimensions in the x and y -directions respectively, b is a spreading parameter and H_0 is the

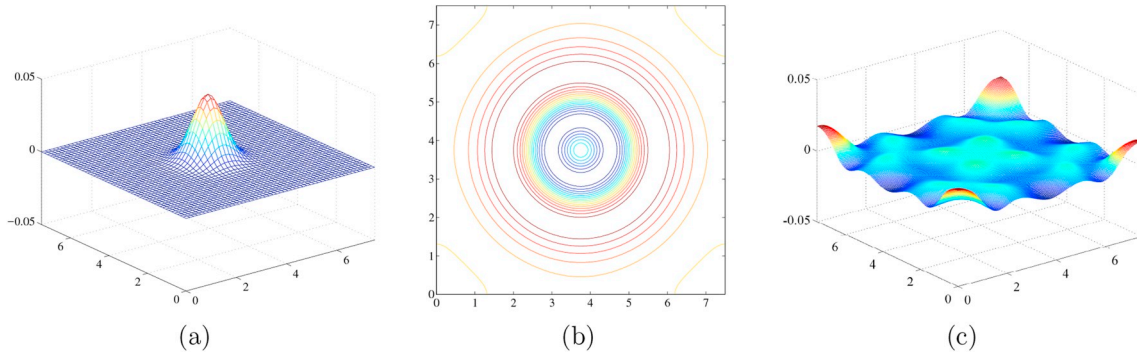


Fig. 4. Evolution of a Gaussian hump in a closed basin: (a) initial symmetric disturbance at $t = 0$ s; (b) ζ -contours at $t = 1$ s and (c) ζ at $t = 50$ s.

initial maximum super-elevation.

The basin under consideration has dimensions $L_x = L_y = 7.5$ m, has a flat, frictionless bottom, and is bounded by vertical, reflective walls on all four sides. The still water depth $h = 0.45$ m, the hump amplitude $H_0 = 0.045$ m and the spreading parameter $b = 2$ m. Wei and Kirby (1995) present the derivation of a linear analytical solution, which at any individual point in the tank at time t with spatial coordinates (x, y) is given by

$$\zeta(x, y, t) = \sum_{n=0}^{\infty} \sum_{m=0}^{\infty} \tilde{\zeta}_{nm} e^{-i\omega_{nm}t} \cos(n\lambda x) \cos(m\lambda y). \quad (26)$$

In the above formula, the amplitude $\tilde{\zeta}_{nm}$ of the n, m -th mode component is given by the expression

$$\tilde{\zeta}_{nm} = \frac{4}{(1 + \delta_{n0})(1 + \delta_{m0})L_x L_y} \int_{-L_x}^{L_x} \int_{-L_y}^{L_y} \zeta_0(x, y) \cos(n\lambda x) \cos(m\lambda y) dx dy, \quad (27)$$

where (n, m) are the wave modes, δ_{nm} is the Kronecker delta function, and the wavelength, $\lambda = \pi/L_x = \pi/L_y$. Each of the (m, n) modes of the waveform has a natural angular frequency, ω_{nm} , given by the dispersion equation, $\omega_{nm}^2 = gk_{nm}\tanh(k_{nm}h)$, where the wavenumber, k_{nm} , is given by $k_{nm} = \sqrt{(n\lambda)^2 + (m\lambda)^2}$.

Using a grid resolution of $\Delta x = \Delta y = 0.0375$ m and a time step, $\Delta t = 0.05$ s, the model is run for 100 s. Both the bed friction coefficient C_f , and the eddy viscosity parameter ϵ , are set to zero. As expected, the waveform propagates outwards in a circular fashion, as illustrated in Fig. 4b, demonstrating the correct handling of the cross-derivative terms.

Fig. 5 provides comparisons between the nonlinear numerical prediction and the linear analytical solution of the free surface time histories at the centre of the tank. The analytical solution is generated by considering 51 wave components in the x - and y -directions (i.e. $m = n = 51$). Overall, there is very close agreement between the numerical and analytical solutions, particularly in the early stages of the wave evolution. As the simulation progresses, the nonlinear properties of the Boussinesq numerical model result in a very gradual phase shift, with very small discrepancies emerging for the peaks and troughs.

Reversibility of the Boussinesq model is verified by running the Gaussian hump simulation for 50 s, at which point the sign of the time step is changed and the simulation is run backwards until $t = 0$ s. The total run time of 100 s provides a very sensitive check on the accuracy of the numerical model. Fig. 6 shows the final surface profile along the basin diagonal at the end of the reversibility test, superimposed on the initial profile. The initial Gaussian hump is recovered, with the very small amplitude loss (≈ 0.2 mm) over the simulation duration due to numerical dissipation in the Boussinesq solver.

4.2. Sloshing in a parabolic basin

Sloshing in a parabolic basin is next simulated, to confirm the

correct implementation of the wetting and drying algorithm. Sampson et al. (2006) derive an analytical solution of the nonlinear shallow water equations for sloshing in a parabolic basin. The bed profile of the parabolic basin is given by

$$z_b(x) = \frac{h_0}{a^2}(x - 0.5L_x)^2, \quad (28)$$

where z_b is uniform with zero slope in the y -direction, L_x is the length of the domain in the x -direction, h_0 is the still water depth at $x = 0.5L$, and a is the width of the basin at elevation $z = h_0$. Sampson et al. give the initial sloping free surface as

$$\eta(x, 0) = h_0 + \frac{a^2\beta^2}{8g^2h_0}(\frac{\tau^2}{4} - s^2) - \frac{\beta^2}{4g} - \frac{\beta s}{g}(x - 0.5L). \quad (29)$$

The analytical solution of the water surface time history is

$$\eta(x, t) = h_0 + \frac{a^2\beta^2 e^{-it}}{8g^2h_0}(-s\tau \sin(2st) + (\frac{\tau^2}{4} - s^2)\cos(2st)) - \frac{\beta^2 e^{-it}}{4g} - \frac{e^{-it/2}}{g}(\beta s \cos(st) + \frac{\beta^2}{2} \sin(st))(x - 0.5L), \quad (30)$$

where β is a velocity constant and s is a constant given by $s = 0.5\sqrt{8gh_0/a^2 - \tau^2}$. τ is a fixed friction parameter related to the bed friction coefficient by $C_f = ht/\sqrt{u^2 + v^2}$.

For the numerical simulation, the computational domain has plan dimensions of $L_x = 220$ m and $L_y = 17.6$ m, with $\Delta x = \Delta y = 1.76$ m. The values of the coefficients are $a = 80$ m, $\beta = 10 \text{ ms}^{-1}$, $h_0 = 80$ m and $\tau = 0.1 \text{ s}^{-1}$. The time step $\Delta t = 0.04$ s and the simulation is run for 80 s.

Excellent agreement is obtained between the analytical and numerical solutions, as shown in Fig. 7. The model accurately predicts the moving wet/dry front, thereby validating the wetting and drying algorithm. The simulation is also run with the basin and initial water surface profile rotated by 90°, i.e. with the bed profile uniform, with zero slope in the x direction, and the parabolic profile occurring in the $y - z$ plane. The results produced for this orientation are identical to those above, allowing for the changed coordinate axis. This benchmark verification test has also been used by other researchers (see e.g. Orszaghova et al., 2012) and (Liang and Borthwick, 2009)).

4.3. Paddle wave generation test

Orszaghova et al. (2012) present a semi-analytical solution for a solitary wave for the one-dimensional Boussinesq equations of Madsen and Sørensen (1992), with a closed form relation between the amplitude of the solitary wave and its celerity. Orszaghova uses this relation to calculate a paddle displacement time-series by solving

$$(x_p)_t = u(x_p, t) = u(x_p - Ct), \quad (31)$$

in which u is the depth-averaged velocity and C is the wave celerity. u is calculated from

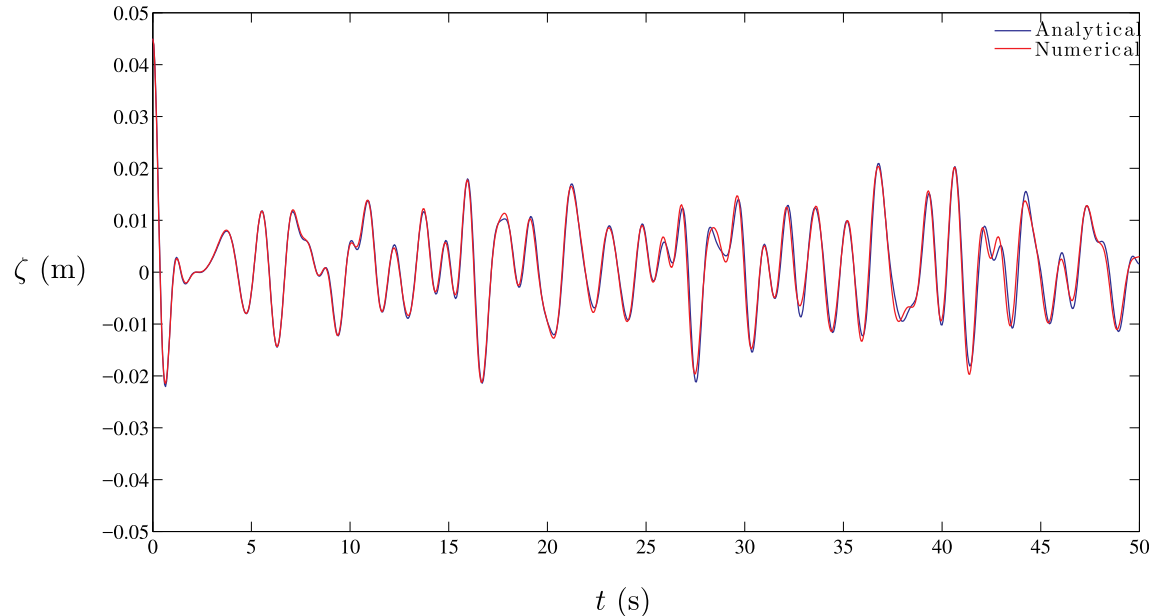


Fig. 5. Evolution of initial Gaussian hump in a closed basin: comparison between the numerical prediction and the analytical solution of the free surface elevation time series at the basin centre point.

$$u = \frac{q}{\zeta + h}, \quad (32)$$

in which q and ζ are the one-dimensional flux and free surface profile calculated using the theory outlined in Orszaghova et al. (2012). Equation (31) is solved numerically using Matlab's in-built ordinary differential equation solver, *ode113*. The paddle signal generated by Orszaghova for a solitary wave of amplitude $A = 0.6$ m in still water depth $h = 1.0$ m is applied to each of the numerical piston paddles in the present model. For this test, a basin of dimensions 50 m by 5 m in the x - and y -directions respectively is utilised, with 26 paddles along the western boundary. The grid spacing is $\Delta x = 0.1$ m and $\Delta y = 0.2$ m, and the time step is set to $\Delta t = 0.006$ s. Bed friction and eddy viscosity parameters are set to zero. Fig. 8 shows the progression of the wave as it moves away from the paddles, along the basin in the x -direction. The surface profiles are stacked with a vertical spacing of 0.6 m to demonstrate that a wave of correct amplitude is generated, and that this amplitude is maintained as the wave propagates. This verification test also confirms that the wave is unaffected as it passes from the moving paddle domain into fixed Boussinesq domain. This demonstrates that the non-uniform finite difference stencils at the interface between the moving and fixed domains are implemented correctly.

4.4. Solitary wave interaction with a conical island

The test case of a solitary wave interacting with a flat-topped conical island has been used as a means of verifying 2DH models by many researchers, including Liang et al. (2012) and Yamazaki et al. (2009). The original experiment is described by Liu et al. (1995), and consisted of a 25 m by 30 m basin with the an island centred at ($x = 13$ m, $y = 15$ m). The base of the island was 7.2 m in diameter, and its side slope was 1V:1H. The conical island was truncated at a height of 0.625 m above the base. Waves were generated using a directional spectral wave generator installed on the long axis of the basin. In the experiments, three solitary waves were considered with height to depth ratios of $\varepsilon = A/h = 0.05, 0.1$, and 0.2 , in water of depth $h = 0.32$ m. Gauges to measure the free-surface displacement were positioned at various locations including those shown in Fig. 9a.

For the numerical simulation, a solitary wave with $\varepsilon = 0.096$ in a still water depth $h = 0.32$ m is considered. A value of 0.096 rather than 0.1 is used because the resulting wave is a better match for the data measured at Gauge 1, and therefore gives a better representation of the incident wave. This is also the approach taken by Yamazaki et al. (2009). The solitary wave is generated by calculating a paddle signal according to the procedure of Orszaghova et al. (2012) outlined in Section 4.3. Grid spacings of $\Delta x = \Delta y = 0.05$ m are implemented in the model with time step $\Delta t = 0.01$ s. A C_f value of 0.008 is used.

Fig. 9b, c, and d present the evolution of the wave free-surface as it

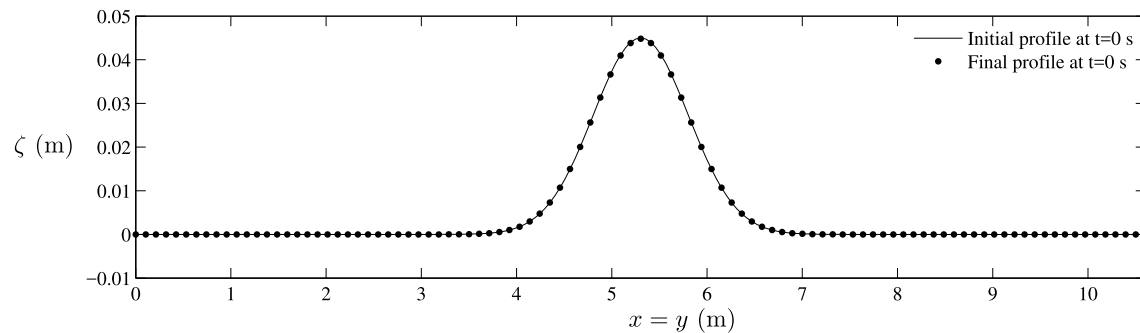


Fig. 6. Evolution of initial Gaussian hump in a closed basin: reversibility check - initial free surface profile at $t = 0$ s and final profile at $t = 0$ s after forward and reverse simulation.

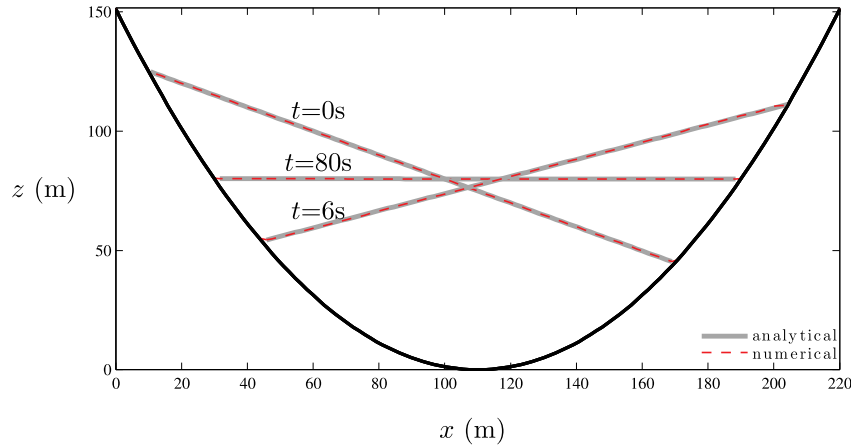


Fig. 7. Sloshing in a parabolic basin: analytical (Sampson et al., 2006) and numerical free surface profiles at times $t = 0, 6$, and 80 s.

interacts with the conical island. The wave front begins to curve as it approaches the island, and generates high run-up on the front face (Fig. 9b). The wave splits either side of the island (Fig. 9c), following which the two waves collide on the lee slope, generating another high run-up event (Fig. 9d). The large run-up events on either side of the island are of similar magnitude. Fig. 10 presents time series of the experimental measurements and numerical predictions of the free surface at the gauge locations shown in Fig. 9a. There is generally good agreement between the measured and predicted data, in particular as the wave approaches the island. Discrepancies are evident after the main wave passes each gauge, particularly at Gauge 6. This may be due to swash zone effects not being fully represented by the wetting and drying scheme, as noted by Liang et al. (2012).

5. Results

5.1. Nearshore circulation at a sinusoidal beach

In order to determine whether the model is capable of simulating near-shore circulation, the laboratory experiment carried out by Da Silva Lima (1981) is considered. In his experiment, da Silva Lima constructed a plywood sinusoidal beach in a wave basin and measured the wave heights and period-averaged currents that resulted from paddle-generated regular waves travelling normal to the beach. These data have been used by a number of other researchers to verify numerical models, e.g. (Park and Borthwick, 2001) and (Rogers et al., 2004).

The still water depth for da Silva Lima's experiment is given by

$$h(x, y) = \begin{cases} [x - 0.75 \sin(\frac{\pi x}{4.36}) \sin(\frac{2\pi y}{\lambda})]s & 0 \leq x \leq 4.36 \text{ m} \\ x s & -0.7 \leq x \leq 0 \text{ m} \\ h_0 & x > 4.36 \text{ m} \end{cases} \quad (33)$$

where x is the distance offshore from the still water line, y is the alongshore distance with a range of $1.5\text{--}4.5$ m, $h_0 = 0.218$ m is the still water depth offshore of the toe, $s = 0.05$ is the slope of the plane beach and $\lambda = 6$ m is a parameter known as the rip current spacing. Applying (33) to a 6 m long and 3 m wide numerical basin results in the bathymetry shown in Fig. 11.

5.1.1. Eddy viscosity and bed friction

In addition to a constant eddy viscosity model, the non-uniform eddy viscosity model of Thornton (1970) (and also described by Park and Borthwick (2001) and Rogers et al. (2004)) is implemented for comparison. Here, the eddy viscosity is given by

$$\varepsilon = M_T A_b \tilde{u}_{\max} \quad (34)$$

where M_T is a dimensionless mixing parameter, and A_b is the excursion length of the orbital motion at the bed, given by

$$A_b = \frac{a}{\sinh(kh)} = \frac{\tilde{u}_{\max} T}{2\pi}, \quad (35)$$

in which a is the wave amplitude and T is the period. The maximum wave particle velocity at the bed is

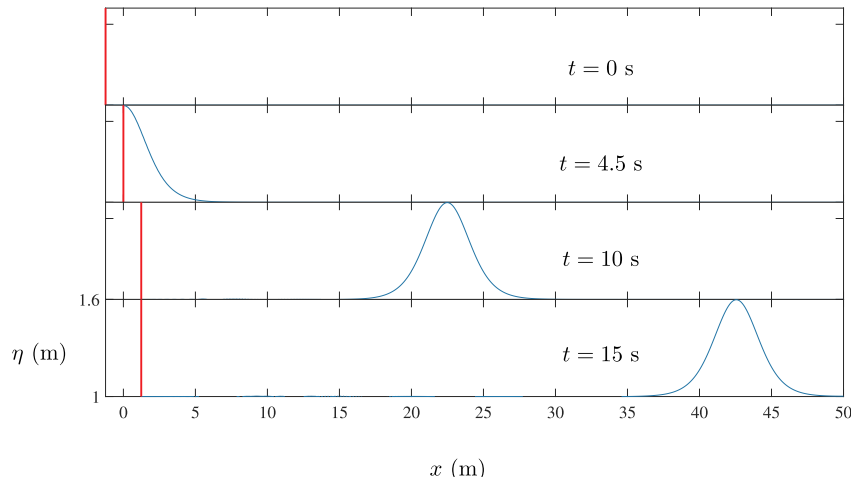


Fig. 8. Solitary wave generated by numerical piston paddles: side-on view of stacked surface water profiles.

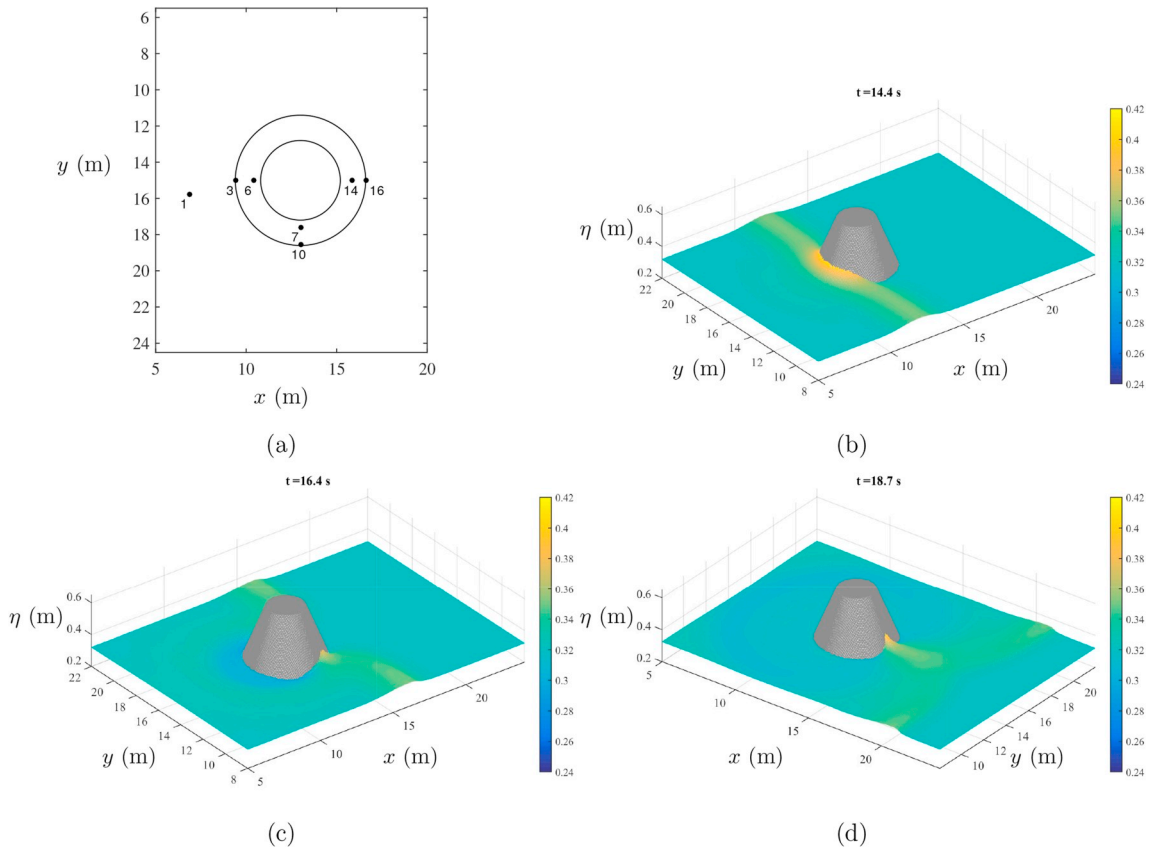


Fig. 9. Solitary wave interaction with a conical island: (a) gauge locations; 3D visualisation of numerically predicted water surface elevations at (b) $t = 14.4$ s, (c) $t = 16.4$ s, and (d) $t = 18.7$ s.

$$\bar{u}_{\max} = \frac{2\pi a}{T \sinh(kh)}, \quad (36)$$

noting that u_{\max} is derived from linear wave theory, whereas (u, v) in the model are calculated from the Boussinesq and nonlinear shallow water equations.

The bed friction coefficient C_f is calculated following the method of Rogers et al. (2004) who references the formula of Jonsson (1966)¹ which is a function of both wave and current bed friction coefficients, \tilde{C}_f and C_{fcur} :

$$C_f = \frac{\tilde{C}_f + \alpha C_{fcur}}{1 + \alpha}, \quad (37)$$

where α is a weighting coefficient given by

$$\alpha = \frac{\sqrt{u^2 + v^2}}{\bar{u}_{\max}}. \quad (38)$$

\tilde{C}_f and C_{fcur} are calculated using empirical expressions based on experimental data. The wave friction factor is determined using Jonsson's formula,

$$\tilde{C}_f = \exp(5.213(\frac{A_b}{R_h})^{-0.194} - 6.67), \quad (39)$$

where R_h is the roughness height. The current friction factor is calculated from the expression obtained by Bijker (1966)².

$$C_{fcur} = 0.016(\frac{R_h}{h})^{\frac{1}{3}} \quad (40)$$

5.1.2. Numerical simulation

The numerical simulation is carried out on a grid of size $\Delta x = \Delta y = 0.05$ m using a time step of $\Delta t = 0.005$ s. Regular waves are generated using the paddles with a wave amplitude $a_0 = 0.0309$ m, period $T = 0.76$ s and incident wave angle $\theta = 0^\circ$. The water depth offshore of the beach toe is $h_0 = 0.218$ m. The minimum water depth is set to 1 mm, to limit unrealistically high velocities at the shoreline, and the simulation is run for 100 s. Three cases are considered: Case A uses a constant eddy viscosity of $\varepsilon = 0.005$ m²/s with a fixed value of $C_f = 0.025$; Case B implements the variable eddy viscosity model outlined in Section 5.1.1 with $M_T = 1.0$ and $R_h = 0.001$ m; and Case C sets $\varepsilon = 0$ m²/s and $C_f = 0.025$.

For Cases A and B, the circulation pattern is established by $t \approx 20$ s, and the current velocities are stable by $t \approx 50$ s. Both cases produce broadly similar results - a clockwise rotating primary circulation cell offshore of the middle of the basin. Case A is characterised by high shoreline velocities and a relatively weak primary gyre, whereas the flow in the primary gyre in Case B is significantly stronger while the shoreline velocities are close to zero. The variable viscosity and bed friction model (i.e. Case B) results in relatively high values of ε ($\approx 0.2 - 0.5$ m²/s) near the shoreline leading to low velocities in this region, while offshore, $\varepsilon \approx 0$ m²/s. Fig. 13 shows the period-averaged velocity vectors (averaged over a single wave period) at $t = 60$ s for Cases A and B, which illustrate the circulation patterns predicted by the numerical model. Data are plotted at every fourth grid point for ease of visualisation.

In this case study, the free surface slope does not exceed the threshold of 0.4, and so the switching criterion is based on the depth to wavelength being 1/20. The dispersive terms of the Boussinesq equations are gradually ramped down approaching the switch point, $x_{Bswitch}$. The resulting loss in energy translates into a pumping action that helps drive the gyre. The amplitude of the wave field at $t = 60$ s and the setup

¹ Referenced by (Jonsson, 1966) but full text not available

² Referenced by (Jonsson, 1966) but full text not available

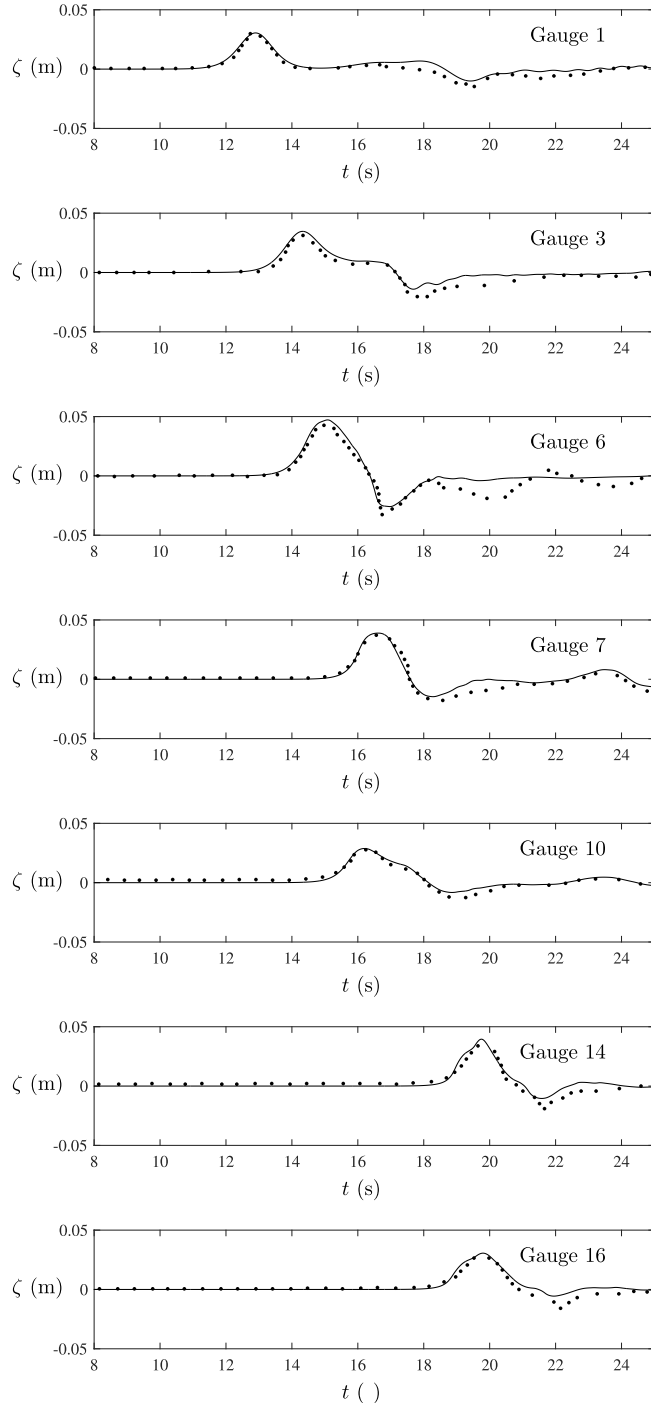


Fig. 10. Solitary wave interaction with a conical island: experimental gauge data from Liu et al., 1995 (dots) and numerically predicted free-surface time series (solid line).

of the mean water level (obtained by averaging the time series from $t = 60$ to 65 s) are shown in Fig. 14a and b. This figure indicates that the surf zone extends from ≈ 1 m from the shore close to the bed trough (at the southern boundary) and almost 2 m from the shore close to the bed cusp (northern boundary). A small hotspot of anomalous wave amplitude (and setup) occurs close to the initial shoreline near the north wall in Fig. 14; this could be related to the very small local depth.

For very small waves, the Boussinesq formulation may be valid all the way to the beach. Therefore, the validity of basing the switch only on the shallowness parameter, without taking nonlinearity into account, is considered by performing a sensitivity analysis on the limiting

value of h/L . Fig. 15a and b presents the circulation patterns predicted by the model at $t = 60$ s for a switching criterion based on values of h/L of $1/30$, and $1/50$. Implementing this criterion has the effect of slightly shifting the main gyre towards the beach. Further decreasing the limiting shallowness parameter (e.g. to $1/60$) has little impact, as the numerical model requires a minimum cross-shore width between the switch point and the wet/dry front to ensure dry cells are not fed into the Boussinesq solver.

Setting $\epsilon = 0 \text{ m}^2/\text{s}$ in Case C, while producing reasonable predictions of the evolving water surface profile, leads to the current field appearing somewhat chaotic, with no settled circulation pattern developing. In a paper describing Boussinesq modelling of rip currents, Chen et al. (1999) attribute this phenomenon to the absence of a model for sub-grid turbulent processes. They conclude that a turbulence model is necessary to account for the influence wave-generated current fields has on flow patterns, and achieve good results by implementing a Smagorinsky-type turbulence model in their fully nonlinear Boussinesq equation set. Chen et al.'s conclusions are confirmed by the present research.

In his experiments, da Silva Lima reports the centroid of the primary gyre as being located approximately 1.7 m offshore of the still water line in the x -direction, and approximately 2.0 m from the northern boundary in the y -direction, as shown in Fig. 12. While the numerical model predicts the circulation pattern with reasonable accuracy, the location of the main gyre is approximately 1.2 m further offshore compared with the experimental results, for both Cases A and B. There are a number of possible reasons for this, including the calibration of the model, and how the switch between the Boussinesq and shallow water equation sets is applied. The equation set switch is triggered by either the slope of the water surface reaching a certain limit, or by the shallowness parameter μ , i.e. the ratio of the water depth to the wavelength. As alluded to previously, in the numerical simulation, the free surface slope does not exceed the set threshold of 0.4, so the switch is determined by the most offshore location where $\mu \leq 1/20$, which in this case is located at $x = 1.65$ m and $y = 1.5$ m, along the northern boundary of the basin. Ideally, the switch point would follow the contours of the beach, varying from $x = 1.65$ m at the northern boundary, between the 0.16 and 0.173 m contours in Fig. 11, to $x \approx 0.7$ m at the southern boundary. In the numerical model, onshore of $x = 1.65$ m, the shallow water equations are applied uniformly across the numerical domain, despite the area of deeper water between 0.7 m and $x = 1.65$ m offshore of the still water line, and $y = 2$ m and $y = 4.5$ m. As a result, wave-current interaction is not adequately represented in this region because the governing shallow water equations are unsuited to this purpose. This is most likely the main reason for the shift in the centroid of the main gyre to a position further offshore than observed in the laboratory experiments.

It may well be that the hydrostatic assumption underpinning the shallow water equations may have contributed to the rather poor representation of secondary circulation cells. A non-hydrostatic model such as that of Antuono et al. (2012, 2017) Antuono and Brocchini (2013), Antuono et al. (2017) could well provide more accurate predictions of secondary gyres, given that such a model includes more of the physics, in particular hydrodynamic pressure which would affect the current-driving mechanisms in the swash zone. Moreover, the present model would benefit from a two-dimensional switch between equation sets, where the interface between the Boussinesq and shallow water domains can follow the bed contours, rather than a straight line in the y -direction across the basin. A curved interface between the domains may be facilitated by switching to a fully finite volume scheme, rather than the coupled finite difference and finite volume scheme proposed herein.

Model calibration may also be a factor affecting the results. Whereas the parameters, C_f and ϵ were varied for Case A, and similarly M_T and R_h for Case B, a detailed parameter study was not carried out. The impact of the value of the local free surface slope limit Θ was

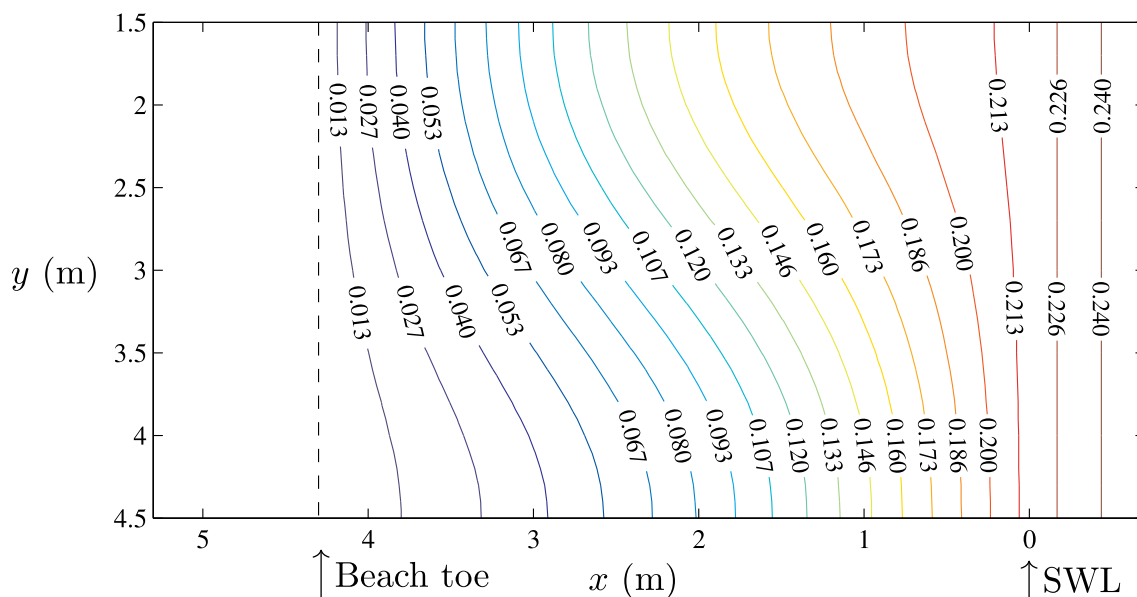


Fig. 11. Contour plot illustrating sinusoidal beach bathymetry.

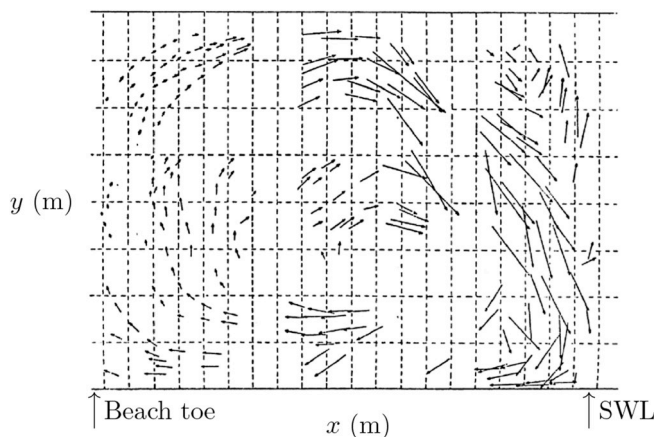


Fig. 12. Nearshore circulation at a sinusoidal beach: Experimental velocities and measurement grid ($\Delta x = 0.2$ m, $\Delta y = 0.375$ m) from Da Silva Lima (1981).

investigated by applying a range of values between 0.3 and 0.5, however this did not produce any discernible change in the predicted circulation pattern. Improved results may be achieved with a more sophisticated turbulence model.

5.2. Nearshore circulation at a tri-cuspate beach

Cuspate beaches represent a category of rhythmic shorelines commonly found at the coast, formed by the interaction between waves, currents and sediment. Borthwick and Foote (2002) present a series of laboratory experiments carried out at the UK Coastal research facility (UKCRF) to investigate the hydrodynamics of regular wave interaction with a fixed cuspate beach. For the experiments, a sinusoidal cuspate beach was constructed on the upper section of an otherwise 1:20 plane beach. Borthwick and Foote investigated the rip currents and circulation cells resulting from regular waves travelling normal to the cuspate beach, and the meandering longshore currents formed when the waves approach the shore at an oblique angle. Digital image analysis of video footage of neutrally buoyant markers was used in the experiments to determine the horizontal spatial patterns of the wave-induced currents, and measurements were also taken of the wave height field and the vertical structure of the rip and nearshore currents. The experimental data obtained have been used by other researchers to verify numerical models, such as by Park and Borthwick (2001) and Rogers et al. (2004).

To investigate further the ability of the numerical model to simulate nearshore circulation over more complex bed topography, the model is applied to Borthwick and Foote's experiment involving regular waves travelling normal to the cuspatte beach (Case B in their paper). The wave basin at the UKCERF has dimensions of 27 m cross-shore and 35 m

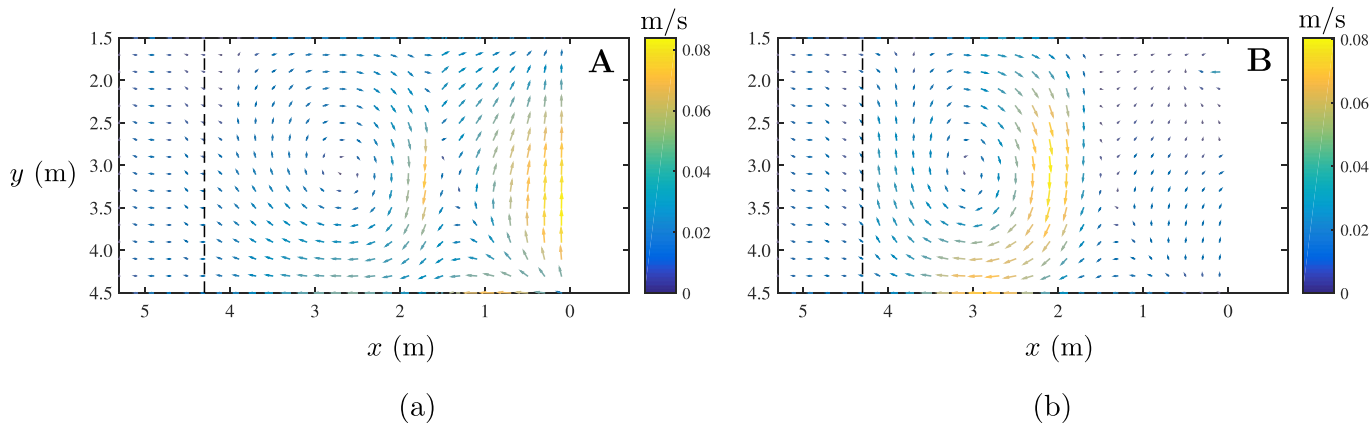


Fig. 13. Nearshore circulation at a sinusoidal beach: period-averaged velocity vectors at $t = 60$ s for (a) Case A and (b) Case B.

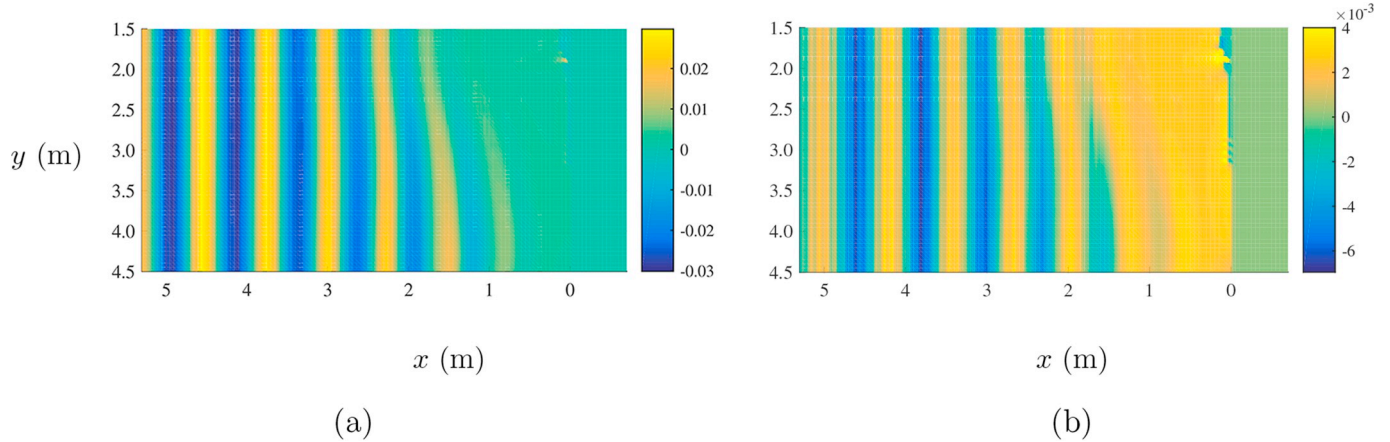


Fig. 14. Nearshore circulation at a sinusoidal beach (Case B): (a) wave field amplitude at $t = 60$ s; and (b) setup.

alongshore with a working area of 20 m by 15 m. Waves are generated using 72 paddle wave-makers that can vary the angle of incidence from 0° to 30° . The beach toe is located 8.33 m from the paddles. At the cusps, the still water depth is given by

$$h(x, y) = s \left((x_L - x) - A \sin \left[\frac{\pi(x_L - x)}{x_L} \right] \left\{ 1 + \sin \left[\phi + \frac{2\pi y}{R} \right] \right\} \right) \quad (48)$$

In the above formula, s is the slope of the underlying plane beach, x_L is the cross-shore length of an individual cusp, x is the distance onshore from the toe of the cusp, A is an amplitude related to the cusp height, ϕ is a phase angle, y is the distance alongshore from the edge of the cusps, and R is the longshore length of an individual cusp. The values ascribed to the parameters for the numerical simulation are $s = 0.05$, $x_L = 5$ m, $A = 0.75$ m, $\phi = 3\pi/2$, and $R = 4$ m. The resulting bathymetry is illustrated in Fig. 16.

The wave conditions simulated by the numerical model are regular waves with period $T = 1.2$ s, offshore height $H_0 = 0.125$ m ramped up over a period of 10 s, and incident wave angle $\theta = 0^\circ$. The numerical basin has dimensions of 20 m by 22 m in the x - and y -directions respectively, with $\Delta x = \Delta y = 0.11$ m. The time step is set to $\Delta t = 0.01$ s and the simulation end time is set to 100 s. A constant eddy viscosity model is implemented, with $\varepsilon = 0.007$ m²/s. The bed friction coefficient C_f is ramped down linearly from $t = 0$ to 10 s from an initially high value of 0.1 to target values of $C_f = 0.001$ at the cusps, and 0.02 elsewhere in the basin, in order to increase the model stability.

By $t \approx 20$ s, a circulation pattern begins to emerge, and is properly established by $t \approx 28$ s. Fig. 17b shows the period averaged velocity

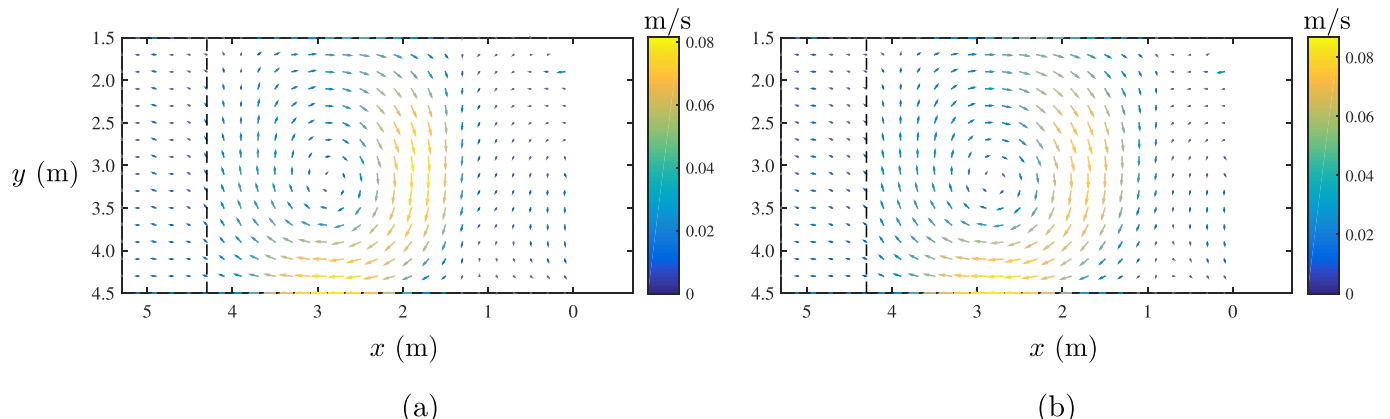


Fig. 15. Nearshore circulation at a sinusoidal beach: period-averaged velocity vectors at $t = 60$ s for Case B with switching criterion (a) $h/L = 1/30$ and (b) $h/L = 1/60$.

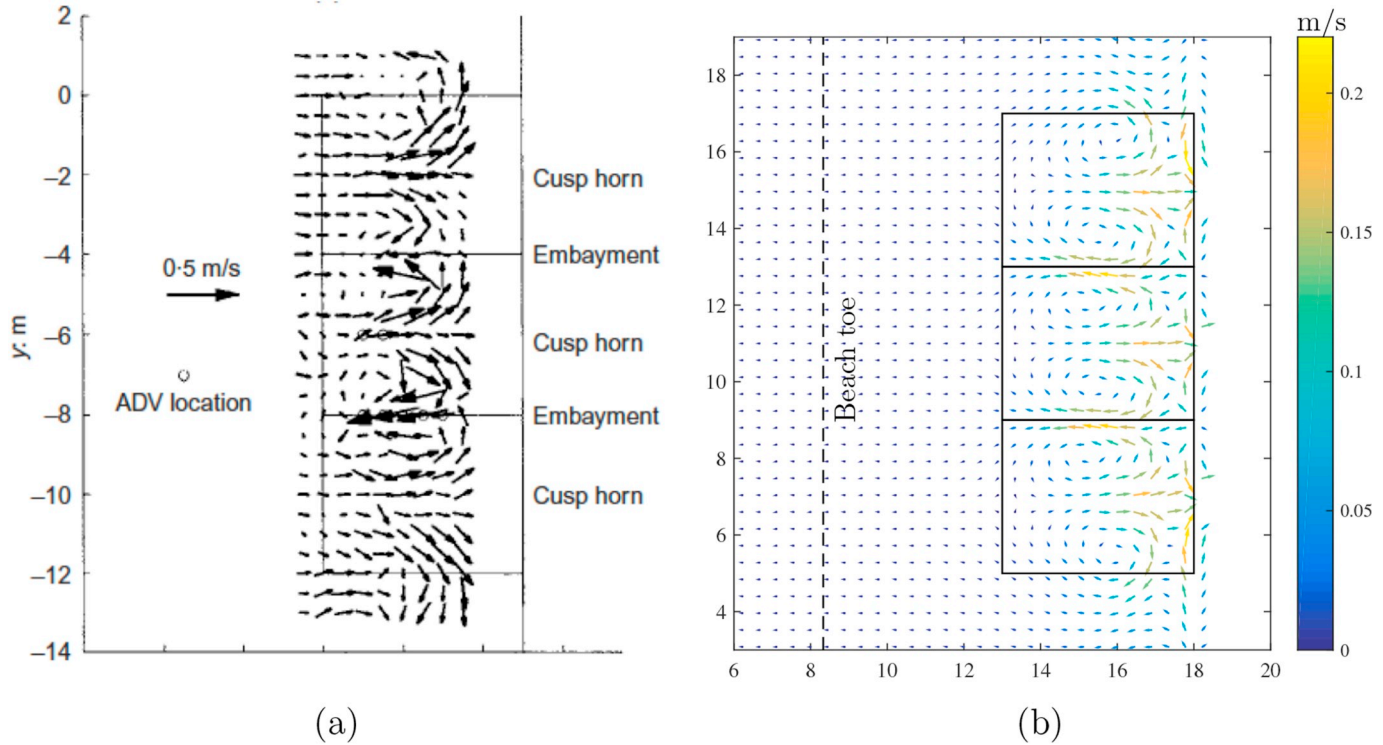


Fig. 17. Tri-cuspate beach: Period-averaged velocity field obtained (a) experimentally by interpolating measured velocities of floats (Borthwick and Foote, 2002), and (b) by the numerical model ($t = 60$ s). The boxed areas on each subfigure represent the three cusps.

defined. This feature of the numerical results is most likely due to the shallow water equations governing in this region. The high shoreline velocities which characterise the constant eddy viscosity simulation of circulation at the half-sinusoidal beach in Section 5.1 are again present here, suggesting the need for a more sophisticated method of calculating C_f in this region.

In the numerical simulations, different values of C_f were tested in the range 0.001–0.01 at the cusps and between 0.01 and 0.03 in the rest of the domain, based on Borthwick and Foote's description of the construction of the cuspate beach. The eddy viscosity parameter ϵ was varied from $0 \text{ m}^2/\text{s}$ to $0.01 \text{ m}^2/\text{s}$. For values of ϵ below $0.007 \text{ m}^2/\text{s}$, it was found that a stable circulation pattern failed to develop, again highlighting the need for an adequate representation of turbulent processes in the numerical scheme. However, for higher values of ϵ , it was found that while the stable circulation patterns developed as described previously by Borthwick and Foote, the velocities were very low, indicating excessively high energy losses.

Neither the sinusoidal or tri-cuspate beach numerical simulations predicted waves with a free-surface slope of $\Theta > 0.4$, therefore for both of these cases, the switch between equation sets was triggered by the shallowness parameter, set to $\mu = 1/20$. As described in Section 3.4, the dispersive terms are ramped down over half a wavelength approaching the switch. This effectively introduces loss of wave height, triggering radiation stresses needed to pump the wave-induced currents. The sensitivity of the shallowness parameter for the tricuspidate beach test was assessed in a similar manner to the half-sinusoidal beach case, by setting $\mu = 1/30$ and $1/50$, however, this did not produce any discernible change in the circulation pattern predicted by the model. By setting $\epsilon = 0 \text{ m}^2/\text{s}$, i.e. Case C in the sinusoidal numerical simulation, Θ was exceeded but as discussed previously, a stable circulation pattern failed to develop. Further research is needed to find a method that can model turbulent processes without excessive energy dissipation, but produces realistic flow patterns.

5.3. Interaction of a uni-directional focused wave group with a plane beach

Experiments undertaken at the UK Coastal Research Facility (UKCRF) using focused wave groups are described by Hunt (2003) and Hunt-Raby et al. (2011), where NewWave theory was implemented to generate 32 different focused wave groups with varying amplitudes and phases. The wave basin at the UKCRF had internal plan dimensions of $20 \text{ m} \times 36 \text{ m}$ in the x - and y -directions respectively. Waves were generated by 72 independently operated piston paddles, each 0.5 m wide and 1.5 m high. The toe of a 1:20 plane beach was located 8.33 m from the paddles. The water surface elevation in the UKCRF experiments was measured using calibrated wave gauges positioned both offshore and in the surf zone. Measurements were taken by Hunt and co-workers at 250 mm intervals along the centre-line of the basin, from 1.5 m offshore of the beach toe ($x = 6.83 \text{ m}$) to $x = 18.33 \text{ m}$.

The numerical model is used to simulate WG1 of the UKCRF tests: a crest-focused wave group with linear focus amplitude $A_f = 0.114 \text{ m}$, focus location at the beach toe ($x = 8.33 \text{ m}$), propagating over a flat bed followed by a plane beach. Still water depth at the paddles is $h = 0.5 \text{ m}$. The wave amplitude selected is the largest in the series of experiments undertaken at the UKCRF. The wave group is generated numerically using the paddle displacement signal from the laboratory experiments, shown in Fig. 18. We note that the horizontal displacements of the paddle are larger than the peak water surface motion at the focus point. The actual (laboratory) paddle signal was calculated at a temporal resolution of $\Delta t = 0.05 \text{ s}$, and so is interpolated to obtain a signal with the desired computational time step of $\Delta t = 0.007 \text{ s}$. To generate a normally incident wave group, the same signal is applied across all paddles in the numerical model. Although the UKCRF basin has a cross-shore dimension of 36 m , the numerical basin is set to 1 m wide to reduce the computational load, while the onshore dimension in the x -direction is set to 22 m . Thus the computational domain is $22 \text{ m} \times 1 \text{ m}$ and mimics a wave flume rather than the whole basin, which is sufficient for modelling waves travelling normal to the beach. The grid size is $\Delta x = \Delta y = 0.04 \text{ m}$, with time step $\Delta t = 0.007 \text{ s}$ and the simulation is run

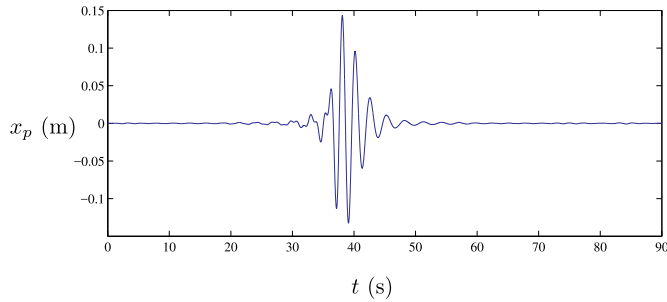


Fig. 18. Paddle displacement time series for uni-directional focused wave group in the UKCRF (WG1).

for 90 s, which corresponds to the total paddle signal duration. The eddy viscosity parameter ϵ is set to zero and the bed friction coefficient $C_f = 0.008$.

Fig. 19 presents plots of the predicted free-surface profile at four different times, showing the evolution of the focused wave group as it propagates up the beach. The red line indicates the paddle position, while the dashed green line represents the switch point between the governing Boussinesq (BE) and nonlinear shallow water (NSWE) equation sets. The switch point is determined by calculating the local slope of the water surface (Equation (23)). In this case, the switch point is set to one quarter of a wavelength offshore of the most offshore location where the threshold slope of 0.4 is exceeded. The wavelength of the wave where the slope threshold is exceeded is determined by a down-crossing method.

Fig. 20 compares the experimentally measured and numerically predicted free surface elevation time series at 6 wave gauge locations along the basin centreline. Leading waves in the wave group are predicted to very high accuracy across all the wave gauge locations. In the deeper water, before the waves break, the numerical model under-predicts the amplitude of the central wave crest, and over-predicts the troughs either side, in particular the trailing trough (see Fig. 20a and b). The wave breaking location, and the propagation of broken waves is predicted with reasonable accuracy. A slight phase lag in the propagation of the third and fourth bores can be seen in Fig. 20c to Fig. 20f,

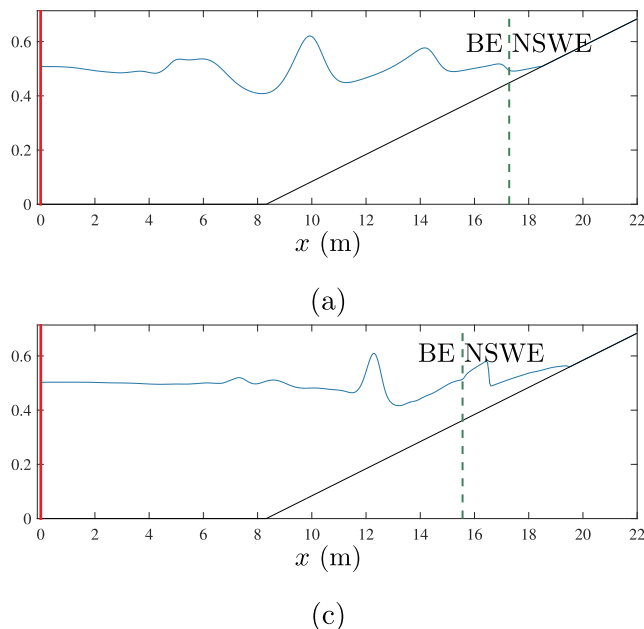


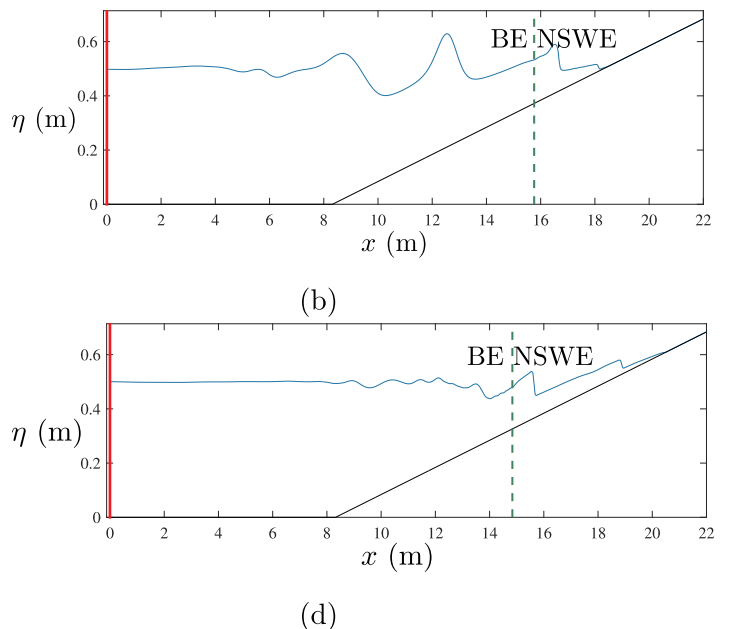
Fig. 19. Numerically predicted water surface elevation profiles (side-on view) in the UKCRF at (a) $t = 45.5$ s; (b) $t = 46.9$ s; (c) $t = 49$ s; and (d) $t = 51.1$ s. The green dotted line represents the switch point between Boussinesq (BE) and nonlinear shallow water (NSWE) equation sets. (For interpretation of the references to colour in this figure legend, the reader is referred to the Web version of this article.)

where the numerically predicted bores appear to travel slower than the waves observed in the laboratory. In general, the mismatch between the numerical prediction and the experimental data mirrors that reported by Orszaghova (2011) for the one-dimensional model, and may be attributed to limitations in the underlying shallow water equations. The speed of propagation (phase speed or celerity) of linear surface gravity waves in shallow water ($kh < \pi/10$) is given by $c = \sqrt{gh}$; however research has shown that this shallow water approximation under-predicts the observed phase speed of waves in the surf zone in both field observations (e.g. (Inman et al., 1971), (Thornton and Guza, 1982), (Martins et al., 2015)) and laboratory experiments (e.g. (Svendsen et al., 1978), (Stive, 1980), (Catálan and Haller, 2008)). Several researchers (e.g. (Schäffer et al., 1993) and (Madsen et al., 1997)) have used a modified shallow water approximation of the phase speed in the surf zone given by $c = a\sqrt{gh}$, where a is a constant to be determined and typically has a value of $a = 1.3$. This value is consistent with surf zone measurements made in the laboratory by (Stive, 1980).

Fig. 21 presents space-time plots of the wave group as it propagates up the beach. Presentation of the data in this way allows an overall comparison to be made between the numerical prediction and the gauge data. The central crest (shown in yellow) and the troughs on either side (dark blue) are clearly visible. Dispersion is evident as the wave group propagates up the beach, and breaking can be identified in the numerical $x - t$ plot by a sharp drop in amplitude at $x \approx 15.5$ m for the central crest, and at $x \approx 13.5$ m for the trailing crest. This feature is more difficult to see in the $x - t$ plot of the experimental data due to the low resolution, but in general there is good agreement between the two datasets. Overall, the numerical model performs well, capturing the evolution of the wave group from the paddle face through to wave breaking and formation of bores.

6. Conclusions

This paper presents a two-horizontal-dimensional (2DH) numerical flow solver for modelling the propagation of waves in the coastal zone, from intermediate to zero depth. Pre-breaking, the numerical model is based on the enhanced Boussinesq equation set derived by Madsen and Sørensen (1992). Broken waves propagate as bores and are described in the hybrid model by the non-linear shallow water equations. The switch



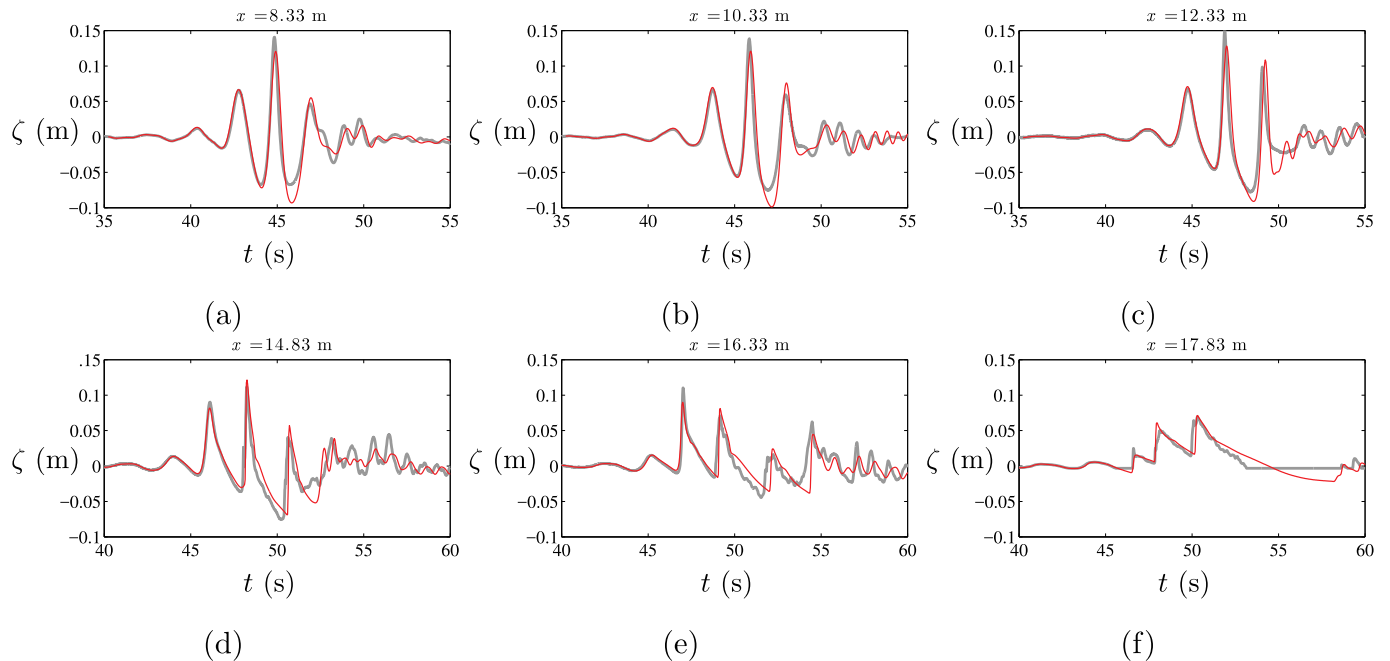


Fig. 20. WG1 - Crest-focused uni-directional wave group time series in the UKCERF: Comparison between measured wave gauge data (thick grey line) and numerical prediction (red line) at selected gauge locations. (For interpretation of the references to colour in this figure legend, the reader is referred to the Web version of this article.)

between the governing equation sets is determined by the most offshore location where the absolute value of the local slope surface vector exceeds a set threshold. The switch is applied uniformly across the domain in the y -direction, with the shallow water equations solved at all points onshore of the switch point in the x -direction, and the Boussinesq equations solved offshore of the switch point. Waves are generated in the model by independently moving numerical piston paddle wave-makers. The deformation of the underlying grid due to the motion back and forth of the paddles is handled by applying a domain-mapping technique in the region adjacent to the paddles.

Different aspects of the numerical model have been verified using a series of benchmark tests. Evolution of sloshing waves, produced by an initial Gaussian hump in a closed, square basin is used to check the correct implementation of the cross-derivative terms in the Boussinesq

equations. Excellent agreement is obtained with the corresponding analytical solution. A reversibility check on the evolution of the Gaussian hump confirms the accuracy of the numerical methods implemented in the model, and demonstrates its conservation properties. Simulation of sloshing in a parabolic basin and comparison of the numerical prediction with the analytical solution of (Sampson et al., 2006) confirm the accuracy of the finite-volume solver and its ability to model the moving wet/dry front. The semi-analytical solution for a solitary wave derived by (Orszaghova, 2011) is used to test the ability of the paddles to generate waves of the desired amplitude. Numerical predictions of the interaction of a solitary wave with a flat-topped conical island were in close agreement with previously published experimental measurements (Liu et al., 1995), confirming that the model correctly simulated two-dimensional inundation and run-up.

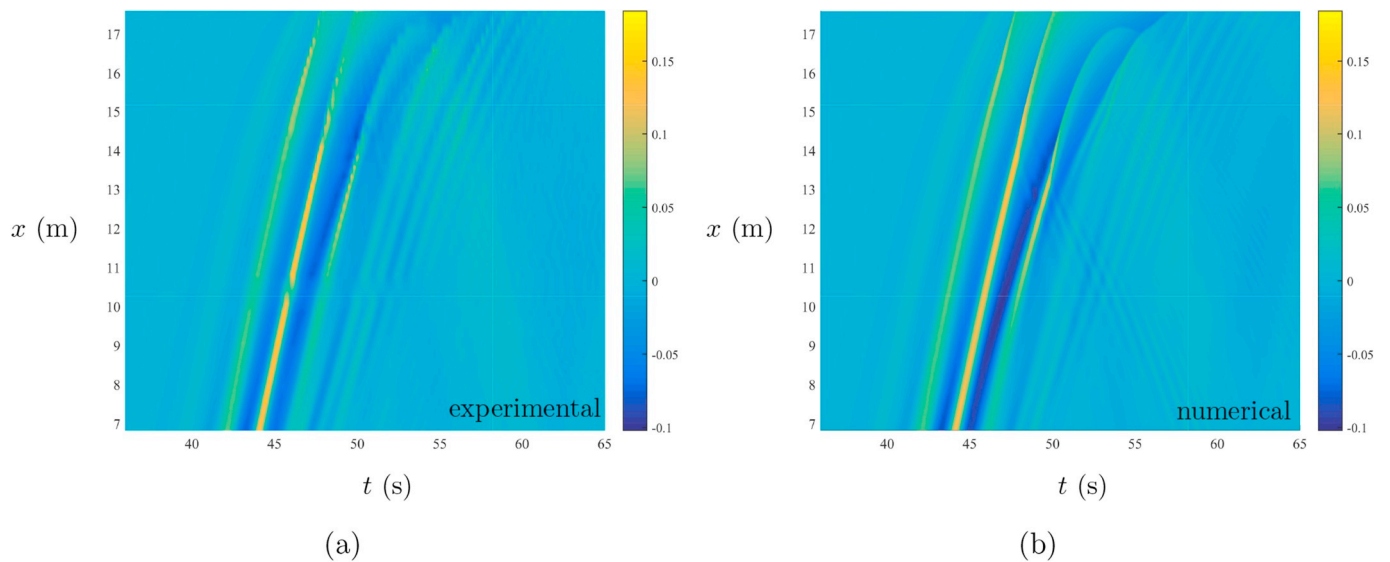


Fig. 21. Space-time ($x - t$) plot of NewWave propagation at a plane beach: (a) measured free-surface; and (b) numerical prediction of free-surface elevation data along basin centreline.

The numerical model has been used to predict nearshore circulation patterns resulting from the interaction of regular waves with non-planar beaches, obtained previously in the laboratory by Da Silva Lima (1981) and Borthwick and Foote (2002). The circulation patterns generated by the laboratory experiments were reasonably well reproduced by the numerical model. Further research is recommended on the implementation of a two-dimensional criterion for the switch between the governing equation sets, as well as a more sophisticated turbulence model. The numerical model has also been used to simulate the propagation of a uni-directional wave group and its interaction with a plane beach. Excellent agreement was obtained between the numerical predictions and previous laboratory measurements of free-surface elevations made at the UKCRF. We believe the present model has considerable potential for modelling multi-directional wave interaction with beaches and coastal structures, and could be used by practitioners to evaluate 2D extreme overtopping and run-up events.

Declaration of interest

None.

Acknowledgements

The authors would like to acknowledge the UK Engineering and Physical Sciences Research Council (EPSRC) and HR Wallingford Ltd. for their co-sponsorship of the U.K. Coastal Research Facility (UKCRF). The multi-cusped beach tests at the UKCRF were funded through EPSRC grant GR/K04125 held at the University of Oxford; Yolanda Foote assisted Alistair Borthwick in the measurements and image processing. The focused wave tests at the UKCRF were carried out as a joint research project between the Universities of Manchester and Oxford. Alison Hunt and Tong Feng carried out the data measurements in the UKCRF, funded through EPSRC grants GR/N21741, GR/N22595, and GR/R05369.

Appendix A. Supplementary data

Supplementary data related to this article can be found at <https://doi.org/10.1016/j.coastaleng.2018.08.014>.

References

- Agnon, Y., Madsen, P.A., Schäffer, H.A., 1999. A new approach to high-order Boussinesq models. *J. Fluid Mech.* 399, 319–333.
- Antuono, M., Brocchini, M., 2013. Beyond Boussinesq-type equations: semi-integrated models for coastal dynamics. *Phys. Fluids* 25 (1), 016603.
- Antuono, M., Soldini, L., Brocchini, M., 2012. On the role of the Chezy frictional term near the shoreline. *Theor. Comput. Fluid Dynam.* 26 (1), 105–116.
- Antuono, M., Colicchio, G., Lugni, C., Greco, M., Brocchini, M., 2017. A depth semi-averaged model for coastal dynamics. *Phys. Fluids* 29 (5), 056603.
- Bellotti, G., Brocchini, M., 2002. On using Boussinesq-type equations near the shoreline: a note of caution. *Ocean Eng.* 29 (12), 1569–1575.
- Bijker, E.W., 1966. The increase of bed shear in a current due to wave motion. In: Proc. 10th Int. Conf. on Coastal Engineering. ASCE, pp. 746–765.
- Boccotti, P., 1983. Some new results on statistical properties of wind waves. *Appl. Ocean Res.* 5 (3), 134–140.
- Borthwick, A.G.L., Barber, R.W., 1992. River and reservoir flow modelling using the transformed shallow water equations. *Int. J. Numer. Meth. Fluid.* 14, 1193–1217.
- Borthwick, A.G.L., Foote, Y.L.M., 2002. Wave-induced nearshore currents at a tri-cuspate beach in the UKCRF. *Proc. Inst. Civ. Eng.: Water Maritime Eng.* 154 (4), 251–263.
- Borthwick, A.G.L., Ford, M., Weston, B.P., Taylor, P.H., Stansby, P.K., 2006. Solitary wave transformation, breaking and run-up at a beach. *Proc. Inst. Civ. Eng.: Maritime Eng.* 159 (MA3), 97–105.
- Boussinesq, J., 1872. Théorie des ondes et des remous qui se propagent le long d'un canal rectangulaire horizontal, en communiquant au liquide contenu dans ce canal des vitesses sensiblement pareilles de la surface au fond. *J. Math. Pure Appl.* 55–108.
- Briganti, R., Musumeci, R.E., Bellotti, G., Brocchini, M., Foti, E., 2004. Boussinesq modeling of breaking waves: description of turbulence. *J. Geophys. Res.: Oceans* 109 (C7).
- Brufau, P., Vázquez-Cendón, M.E., García-Navarro, P., 2002. A numerical model for the flooding and drying of irregular domains. *Int. J. Numer. Meth. Fluid.* 39 (3), 247–275.
- Catálan, P.A., Haller, M.C., 2008. Remote sensing of breaking wave phase speeds with application to non-linear depth inversions. *Coast Eng.* 55 (1), 93–111.
- Chen, Q., Dalrymple, R.A., Kirby, J.T., Kennedy, A.B., Haller, M.C., 1999. Boussinesq modeling of a rip current system. *J. Geophys. Res.* 104 (C9) 20,617–620,637.
- Chen, Q., Kirby, J.T., Dalrymple, R.A., Kennedy, A.B., Chawla, A., 2000. Boussinesq modeling of wave transformation, breaking, and runup. II: 2D. *J. Waterw. Port, Coast. Ocean Eng.* 126 (1), 48–56.
- Da Silva Lima, S., 1981. Wave-induced Nearshore Currents. PhD Thesis. Liverpool University.
- Fitzgerald, C.J., Taylor, P.H., Orszagova, J., Borthwick, A.G.L., Whittaker, C., Raby, A.C., 2016. Irregular wave runup statistics on plane beaches: application of a Boussinesq-type model incorporating a generating-absorbing sponge layer and second-order wave generation. *Coast Eng.* 114, 309–324.
- Gobbi, M.F., Kirby, J.T., Wei, G.E., 2000. A fully nonlinear Boussinesq model for surface waves. Part 2. Extension to O(kh) *J. Fluid Mech.* 405, 181–210.
- Hestenes, M.R., Stiefel, E., 1952. Methods of conjugate gradients for solving linear systems. *J. Res. Natl. Bur. Stand.* 49 (6).
- Hunt, A., 2003. Extreme Waves, Overtopping and Flooding at Sea Defences. DPhil Thesis. University of Oxford.
- Hunt-Raby, A.C., Borthwick, A.G.L., Stansby, P.K., Taylor, P.H., 2011. Experimental measurement of focused wave group and solitary wave overtopping. *J. Hydraul. Res.* 49 (4), 450–464.
- Inman, D.L., Tait, R.J., Nordstrom, C.E., 1971. Mixing in the surf zone. *J. Geophys. Res.* 76 (15), 3493–3514.
- Jalali, M.R., Borthwick, A.G.L., 2017. One-dimensional and two-dimensional Green-Naghdi equations for sloshing in shallow basins. In: Proceedings of the Institution of Civil Engineers-engineering and Computational Mechanics, pp. 1–22.
- Johnson, R.S., 1997. A Modern Introduction to the Mathematical Theory of Water Waves, vol. 19.
- Jonathan, P., Taylor, P.H., 1997. On irregular, nonlinear waves in a spread sea. *Trans. Am. Soc. Mech. Eng.: J. Offshore Mech. Arctic Eng.* 119, 37–41.
- Jonsson, I.G., 1966. *The Friction factor for a Current Superimposed by Waves. 11: Coastal Engineering and Hydraulic Laboratory*. Technical University of Denmark.
- Karambas, T.V., Koutitas, C., 1992. A breaking wave propagation model based on the Boussinesq equations. *Coast Eng.* 18 (1–2), 1–19.
- Liang, Q., Borthwick, A.G.L., 2009. Adaptive quadtree simulation of shallow flows with wet-dry fronts over complex topography. *Comput. Fluids* 38, 221–234.
- Liang, D., Borthwick, A.G.L., Romer-Lee, J.K., 2012. Run-up of solitary waves on twin conical islands using a Boussinesq model. *J. Offshore Mech. Arctic Eng.* 134 (1), 011102.
- Lindgren, G., 1970. Some properties of a normal process near a local maximum. *Ann. Math. Stat.* 1870–1883.
- Liu, P.L.-F., Cho, Y.-S., Briggs, M.J., Kanoglu, U., Synolakis, C.E., 1995. Runup of solitary waves on a circular island. *J. Fluid Mech.* 302, 259–285.
- Madsen, P.A., Schäffer, H.A., 1998. Higher-order Boussinesq-type equations for surface gravity waves: derivation and analysis. *Phil. Trans.: Math., Phys. Eng. Sci.* 356 (1749), 3123–3184.
- Madsen, P.A., Sørensen, O.R., 1992. A new form of the Boussinesq equations with improved linear dispersion characteristics. Part 2. A slowly-varying bathymetry. *Coast Eng.* 18, 183–204.
- Madsen, P.A., Sørensen, O.R., Schäffer, H.A., 1997. Surf zone dynamics simulated by a Boussinesq type model. Part I Model description and cross-shore motion of regular waves. *Coast Eng.* 32 (4), 255–287.
- Madsen, P.A., Bingham, H.B., Schäffer, H.A., 2003. Boussinesq-type formulations for fully nonlinear and extremely dispersive water waves: derivation and analysis. *Proc. Math. Phys. Eng. Sci.* 459, 1075–1104.
- Madsen, P.A., Fuhrman, D.R., Wang, B., 2006. A Boussinesq-type method for fully nonlinear waves interacting with a rapidly varying bathymetry. *Coast Eng.* 53 (5), 487–504.
- Martins, K., Blenkinsopp, C.E., Zang, J., 2015. Monitoring individual wave characteristics in the inner surf with a 2-Dimensional laser scanner (LiDAR). *J. Sens.* 2016.
- McCabe, M.V., Stansby, P.K., Apsley, D.D., 2013. Random wave runup and overtopping a steep sea wall: shallow-water and Boussinesq modelling with generalised breaking and wall impact algorithms validated against laboratory and field measurements. *Coast Eng.* 74, 33–49.
- Nwogu, O., 1993. Alternative form of Boussinesq equations for nearshore wave propagation. *J. Waterw. Port, Coast. Ocean Eng.* 119 (6), 618–638.
- Orszagova, J., 2011. Solitary Waves and Wave Groups at the Shore. DPhil Thesis. University of Oxford.
- Orszagova, J., Borthwick, A.G.L., Taylor, P.H., 2012. From the paddle to the beach - a Boussinesq shallow water numerical wave tank based on Madsen and Sørensen's equations. *J. Comput. Phys.* 231 (2), 328–344.
- Park, K.-Y., Borthwick, A.G.L., 2001. Quadtree grid numerical model of nearshore wave-current interaction. *Coast Eng.* 42 (3), 219–239.
- Peregrine, D.H., 1967. Long waves on a beach. *J. Fluid Mech.* 27 (04), 815–827.
- Rogers, B.D., Borthwick, A.G.L., Taylor, P.H., 2003. Mathematical balancing of flux gradient and source terms prior to using Roe's approximate Riemann solver. *J. Comput. Phys.* 192 (2), 422–451.
- Rogers, B.D., Borthwick, A.G.L., Taylor, P.H., 2004. Godunov-type adaptive grid model of wave-current interaction at cuspathe beaches. *Int. J. Numer. Meth. Fluid.* 46, 569–606.
- Sampson, J., Easton, A., Singh, M., 2006. Moving boundary shallow water flow above parabolic bottom topography. *ANZIAM J.* 47, C373–C387.
- Schäffer, H.A., Madsen, P.A., Deigaard, R., 1993. A Boussinesq model for waves breaking in shallow water. *Coast Eng.* 20 (3–4), 185–202.
- Shewchuk, J.R., 1994. An Introduction to the Conjugate Gradient Method without the Agonizing Pain. School of Computer Science, Carnegie Mellon University.
- Shi, F., Kirby, J.T., Harris, J.C., Geiman, J.D., Grilli, S.T., 2012. A high-order adaptive

- time-stepping TVD solver for Boussinesq modeling of breaking waves and coastal inundation. *Ocean Model.* 43, 36–51.
- Stive, M.J.F., 1980. Velocity and pressure field of spilling breakers. *Coast Eng.* 1980, 547–566.
- Svendsen, I.A., 1984. Mass flux and undertow in a surf zone. *Coast Eng.* 8 (4), 347–365.
- Svendsen, I.A., Madsen, P.A., Buhr Hansen, J., 1978. Wave characteristics in the surf zone. *Coast Eng.* 1978, 520–539.
- Taylor, P.H., Williams, B.A., 2004. Wave statistics for intermediate depth water - NewWaves and symmetry. *Trans. Am. Soc. Mech. Eng.: J. Offshore Mech. Arctic Eng.* 126 (1), 54–59.
- Thornton, E.B., 1970. Variation of longshore current across the surf zone. In: Proc. 12th Conf. Coastal Engineering. ASCE, pp. 291–308.
- Thornton, E.B., Guza, R.T., 1982. Energy saturation and phase speeds measured on a natural beach. *J. Geophys. Res.: Oceans* 87 (C12), 9499–9508.
- Tonelli, M., Petti, M., 2009. Hybrid finite volume - finite difference scheme for 2DH improved Boussinesq equations. *Coast Eng.* 56 (5), 609–620.
- Tonelli, M., Petti, M., 2012. Shock-capturing Boussinesq model for irregular wave propagation. *Coast Eng.* 61, 8–19.
- Tromans, P.S., Anaturk, A.R., Hagemeijer, P., 1991. A new model for the kinematics of large ocean waves-application as a design wave. In: International Society of Offshore and Polar Engineers.
- Wei, G., Kirby, J.T., 1995. Time-dependent numerical code for extended Boussinesq equations. *J. Waterw. Port, Coast. Ocean Eng.* 121 (October), 251–261.
- Wei, G., Kirby, J.T., Grilli, S.T., Subramanya, R., 1995. A fully nonlinear Boussinesq model for surface waves. Part 1. Highly nonlinear unsteady waves. *J. Fluid Mech.* 294 (13), 71–92.
- Whittaker, C.N., Raby, A.C., Fitzgerald, C.J., Taylor, P.H., 2016. The average shape of large waves in the coastal zone. *Coast Eng.* 114 (Suppl. C), 253–264.
- Yamazaki, Y., Kowalik, Z., Cheung, K.F., 2009. Depth-integrated, non-hydrostatic model for wave breaking and run-up. *Int. J. Numer. Meth. Fluid.* 61 (5), 473–497.
- Yoon, S.B., Liu, P.L.-F., 1989. Interactions of currents and weakly nonlinear water waves in shallow water. *J. Fluid Mech.* 205, 397–419.